Dissertation presented to the Instituto Tecnológico de Aeronáutica, in partial fulfillment of the requirements for the degree of Master of Science in the Graduate Program of Engenharia Aeronáutica e Mecânica, Field of Sistemas Aeroespaciais e Mecatrônica.

Willem Pieter Waasdorp

INFLUENCE OF SUBOPTIMALLY FORCED STREAMWISE STREAKS ON THE TURBULENT BOUNDARY LAYER AND SHEAR LAYER

Dissertation approved in its final version by signatories below:

Dr. André V.G. Cavalieri

Advisor

Prof. Dr. Roberto Gil Annes da Silva

Dean for Graduate Education and Research

Campo Montenegro
São José dos Campos, SP - Brazil
2018

Cataloging-in Publication Data
Documentation and Information Division

Waasdorp, Willem Pieter
Influence of suboptimally forced streamwise streaks on the turbulent boundary layer and shear layer / Willem Pieter Waasdorp.
Sï¿½o Josï¿½ dos Campos, 2018.
55f.

Dissertation of Master of Science – Course of Engenharia Aeronáutica e Mecânica. Area of Sistemas Aeroespaciais e Mecatrônica – Instituto Tecnológico de Aeronáutica, 2018. Advisor: Dr. André V.G. Cavalieri.

1. Turbulence. 2. Streaks. 3. Linear stability. I. Instituto Tecnológico de Aeronáutica. II. Title.

BIBLIOGRAPHIC REFERENCE

WAASDORP, Willem Pieter. **Influence of suboptimally forced streamwise streaks on the turbulent boundary layer and shear layer**. 2018. 55f. Dissertation of Master of Science – Instituto Tecnológico de Aeronáutica, São José dos Campos.

CESSION OF RIGHTS

AUTHOR'S NAME: Willem Pieter Waasdorp
PUBLICATION TITLE: Influence of suboptimally forced streamwise streaks on the turbulent boundary layer and shear layer.
PUBLICATION KIND/YEAR: Dissertation / 2018

Willem Pieter Waasdorp
Alameda dos Kings, 134
12.246-370 – São José dos Campos–SP

INFLUENCE OF SUBOPTIMALLY FORCED STREAMWISE STREAKS ON THE TURBULENT BOUNDARY LAYER AND SHEAR LAYER

Willem Pieter Waasdorp

Thesis Committee Composition:

Prof. Dr.	Roberto Gil Annes da Silva	Presidente	-	ITA
Dr.	André V.G. Cavalieri	Advisor	-	ITA
Dr.	Rodrigo Moura		-	ITA
Prof. Dr. Ir.	Andre de Boer		-	UTwente
Dr.	Leandro Dantas de Santana		-	UTwente
Dr. Ir.	Richard Loendersloot		-	UTwente

ITA

Acknowledgments

First of all, I would like to thank both the University of Twente and ITA for providing this unique opportunity to take part in this double degree program.

Next, I would like to thank my advisor, André Cavalieri, who has introduced me to the topic of coherent structures in turbulent flows, and has been a pleasure to work with while providing guidance in the research that I have done. Also to the people in the *caverna*, who it has been a pleasure to lunch, drink coffee and work with.

Thanks to the technicians of the FENG laboratory: Wilson, Rondinele, and Nilton for helping with the setup of the experiments, both making new parts, and major bugfixing.

Lastly, and most importantly, I would like to thank my family, my father, my mother and my brother for their continuous support of my academic career and especially this adventure in Brazil.

"Big whirls have little whirls,
that feed on their velocity,
and little whirls have lesser whirls,
and so on to viscosity."
— Lewis Fry Richardson

Abstract

In this work a modified turbulent boundary layer and shear layer are studied. The base flow is changed by the introduction of spanwise periodic disturbances. An experimental investigation is carried out, where the spanwise periodic disturbances are realised by using an array of cylinders upstream of a backwards facing step. Due to the design of the test section, the disturbances cannot be chosen as the most optimal disturbances. Recent developments have seen the stabilizing effects of streamwise velocity streaks on several different base flows. It is shown that the array of roughness elements incite spanwise periodic disturbances with elongated streamwise presence. It is shown that for large height ($k > \delta$) and small height ($k < \delta$) the streamwise streaks survive the effects of a backwards facing step and are present until at least twelve boundary layer thicknesses from their initiation. Previous research has shown how streaks modulate the spanwise rms profiles in a near wall range for a zero pressure gradient turbulent boundary layer. Streaks resulting from the forcing by the roughness elements show the same type of behaviour on a scale that is comparable to the height of the roughness elements. A loudspeaker is used to force a single phase, single frequency disturbance upstream of the roughness elements. A linear stability analysis is carried out on the shear layer at a distance of one step height downstream from the BFS. The eigenmodes that are found in the stability analysis match with the Fourier modes that result from a phase averaging procedure. The amplitude of the Fourier modes for a baseline case are compared to the forced base flow and show that the streaks have a stabilizing effect on the shear layer, and attenuate velocity fluctuations that are present in the shear layer, while increasing the shear layer thickness. The way in which streaks are studied can be greatly simplified by using roughness elements to force streaks to the desired specification. Another application may be found in the acoustic noise generated by jets. As the fluctuations in the shear layer are attenuated, the shear layer may produce less noise while the increased thickness may allow fluctuations to exist at longer wavelengths and produce a lower noise. An acoustic investigation can provide clarity.

List of Figures

List of Tables

Contents

1 Introduction

Some of the most common phenomena in the modern day aeronautical industry are the effects induced by turbulent separated flows. These include turbulent boundary layer separation (eg. on wings) and turbulent shear layers (eg. engine outflows). Both of these flows have been and still are studied extensively. Flow separation in boundary layers can lead to loss of performance of the flow device, i.e. loss of lift of a wing. The turbulent mixing layer created by the exhaust of a jet engine contributes to the overall airplane noise. Recent developments in the jet engine industry have seen serrated edges added to the nacelles of aircraft jet engines. These modified nacelles introduce a spanwise periodic disturbance in the flow. The way these serrated edges are designed is still mostly empiric. Understanding how these serrated edges change the flow situation and what their effect is based on their design could provide useful in developing a systematic design process for these type of applications.

1.1 Turbulent boundary layer

The turbulent boundary layer has been studied extensively and a great deal of work has been written about it. A great controversy started with the publication of (BARENBLATT, 1993) and (BARENBLATT *et al.*, 1997), who suggested a power law for the description of the mean velocity profile. This triggered a renewed interest and a lot of new work. This new work included diverse projects as the superpipe (ZAGAROLA; SMITS, 1998), very low freestream turbulence windtunnel (OSTERLUND, 1999) and a 27 meter entrance length wind tunnel (NICKELS *et al.*, 2007), all capable of studying high Reynolds number flow. Smits (SMITS *et al.*, 2011) gives a more detailed overview of this development. One of the results is the uncovering of a new class of organized motions that are larger than the characteristic length scale of a flow, so called large scale motions (LSM). Marusic (MARUSIC *et al.*, 2010a) has studied these streamwise velocity streaks and the resulting changes in the fluctuations in different wall distances.

1.2 Backwards facing step

A widely employed geometry to study shear layers and their reattachment is the backwards facing step (BFS). The backwards facing step is a very simple geometry where a sudden expansion of the test section is used to create a shear layer. the classical BFS can be seen in figure 1.1. Because of its simplicity it is easy to study even with little resources, and has been studied for years. A review of research that has been done on the flow reattachment and the BFS configuration has been written by Eaton and Johnston (EATON; JOHNSTON, 1981). The influence of the properties of the separating boundary

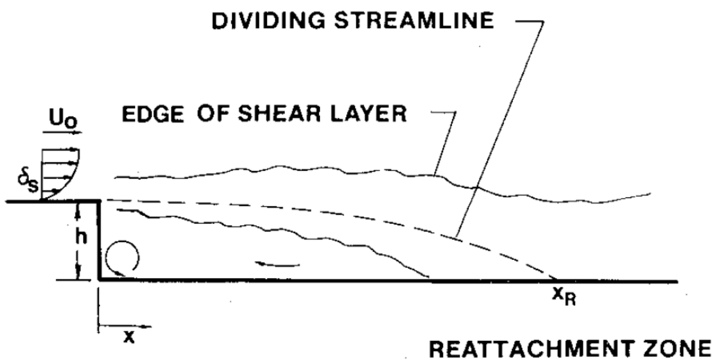

FIGURE 1.1 – Classical Backwards Facing Step configuration, taken from (EATON; JOHNSTON, 1981)

layer has been studied for different laminar boundary layers (SINHA *et al.*, 1982) and turbulent boundary layers (ADAMS; JOHNSTON, 1988a). The influence of the step-height Reynolds number on the reattachment length and wall shear stress has also been studied (ADAMS; JOHNSTON, 1988b)

1.3 Organized motion

In the early 80's of the previous century there was a rise in the understanding of turbulence, but the understanding of fluid mechanics was limited by the presence of turbulence (CANTWELL, 1981). The recognition of organized motion prompted exploration in the application of linear stability theory to the turbulent flows. Spatial stability analysis of a free shear layer profile by Michalke (MICHALKE, 1965) shows good agreement between linear stability theory and experimental data, specifically the phase velocity c_r and growth rate α_i. Where the theory was originally only used on laminar flows to study transition, Crow (CROW; CHAMPAGNE, 1971) applied it to a turbulent jet, and observed the presence of a preferred mode, responding to a low-amplitude periodic exitation. Suggested by Freymuth (FREYMUTH, 1966) and extended by Crow (CROW; CHAMPAGNE, 1971) this these results encourage the use of linear stability models on turbulent flows with a decomposition of the velocity field in a mean, periodic disturbance and incoherent disturbance, where the mean profile is used as the base flow in the stability analysis. Hussain and Reynolds (HUSSAIN *et al.*, 1970) have proposed a decomposition for a signal $f(\underline{x}, t)$ based on the previous description of velocity components. Consider a periodic disturbance, i.e. wave, imposed on the flow in an arbitrary way (e.g. loudspeaker, vibrating ribbon). To extraxt an organized wave motion from the turbulent field, this wave can be used as reference for selective sampling. The proposed decomposition is given in equation 1.1, where $\bar{f}(\underline{x})$ is the mean, $\tilde{f}(\underline{x}, t)$ is the contribution from the artificially forced wave, and $f'(\underline{x}, t)$ is the incoherent part of the signal.

$$f(\underline{x}, t) = \bar{f}(\underline{x}) + \tilde{f}(\underline{x}, t) + f'(\underline{x}, t) \tag{1.1}$$

A phase average can now be calculated as

$$\langle f(\underline{x}, t)\rangle = \lim_{N\to\infty} \frac{1}{N} \sum_{n=0}^{N} f(\underline{x}, t + n\tau) \tag{1.2}$$

with τ the period of the forcing wave. Because the phase average in equation 1.2 is given for a particular phase ϕ the wave component can be derived as

$$\tilde{f}(\underline{x}, t) = \langle f(\underline{x}, t)\rangle - \bar{f}(\underline{x})$$

The wave component $\tilde{f}(\underline{x}, t)$ is periodic by definition and whenever a propagating wave is present in the flow, it should arise from signal $f(\underline{x}, t)$, provided that the used equipment is able to capture the disturbances. After enough averaging iterations the homogeneity of turbulence in time ensures that any disturbances that were not deliberately imposed on the flow will average out, making sure that $\tilde{f}(\underline{x}, t)$ represents a hydrodynamic wave.

The influence of free stream turbulence on the laminar boundary layer has been studied, and spanwsise modulations of the boundary layer thickness have been observed (KENDALL, 1985). The observed disturbances have been named Klebanoff modes, after early observations by Klebanoff (KLEBANOFF, 1971). These results prompted a new direction of research where these Klebanoff modes are forced using spanwise distributed roughness elements.

1.3.1 Flow control

Kendall and Bakchinov (KENDALL, 1990; BAKCHINOV *et al.*, 1995) have observered velocity deficits in the region between the roughness elements, while White (WHITE, 2002) has observed a velocity amplification in this region. Cossu and Brandt (COSSU; BRANDT,

2002) have done numerical investigation of the stabilization of Tollmien-Schlichting waves in the Blasius boundary layer, which have been experimentally verified by Fransson et al (FRANSSON *et al.*, 2004; FRANSSON *et al.*, 2005; FRANSSON *et al.*, 2006).

The effect on the drag reduction of a bluff body using roughness elements in a turbulent boundary layer flow was studied by Pujals (PUJALS *et al.*, 2010), they found that the separation on the rear-end of an Ahmed body is suppressed by the presence of large scale streaks on the topside of the body. Ryan (RYAN *et al.*, 2011) compared the velocity field behind a single cylinder with that behind an array of similar cylinders in a turbulent boundary layer. The velocity deficit is larger behind an array of cylinders and is largest in the spanwise center between two cylinders.

1.4 Goals

The goals of this work are to study the effects of spanwise periodic forcing of the turbulent boundary layer, and the generation of streamwise streaks, on the properties of the turbulent boundary layer and the shear layer induced by a classical BFS configuration.

An existing test-section for the study of the reattachment of a shear layer, detached from a BFS, is adapted to allow for static spanwise periodic forcing. The effects of the forcing on the boundary layer and its characteristics will be studied as well as the influence on the shear layer. A linear stability analysis is performed on the shear layer, in a similar way as in (ORMONDE *et al.*, 2018). It is investigated if the velocity fluctuations in the shear layer are influenced by a linear mechanism.

In this chapter a review of previous work and results is given. In chapter 2 the linear stability theory is explored in more depth and concepts that will be used later are introduced. Code to perform stability analysis is also verified using previous results. Chapter 3 describes the experimental setup that was used to perform experiments, and the decisions that have been made to come to the final design of the experiments. In chapter 4 the experimental results will be shown and discussed. Firstly results for the experiment will be shown in full while later a distinction will be made between the boundary layer and the shear layer. Finally, chapter 5 will give conclusions and a discussion about future research possibilities. There is an appendix, which contains multiple experimental results. In chapter 4 a scope is narrowed to avoid cluttering and to get the clearest results.

2 Linear stability theory

This chapter serves to introduce the subject of linear stability and the concepts of linearization, stability analysis and linear structures. These concepts are introduced here because they serve as foundations for decisions made further on, for both experimental setup, and analysis of the results. It is largely based on the book by Peter Schmid and Dan Henningson (SCHMID; HENNINGSON, 2001).

2.1 Derivation of the Orr-Sommerfeld equation

The general equations of motion for fluids are the Navier-Stokes equations. For an inviscid fluid they are defined as

$$\frac{\partial u_i}{\partial t} = -u_j \frac{\partial u_i}{\partial x_j} - \frac{\partial p}{\partial x_i} + \frac{1}{Re}\nabla^2 u_i \tag{2.1}$$

$$\frac{\partial u_i}{\partial x_i} = 0 \tag{2.2}$$

where u_i is the i'th velocity component, x_i is the i'th spatial coordinate, p is the pressure, and Re is the Reynolds number. Equation 2.1 describes conservation of momentum, and equation 2.2 describes conservation of mass. Boundary and initial conditions will be applied in the form

$$\begin{aligned} u_i(x_i, 0) &= u_i^0(x_i) \\ u_i(x_i, t) &= 0 \qquad \text{on solid boundaries.} \end{aligned}$$

To nondimensionalize the equations, a velocity scale is chosen based on the base flow. Only boundary layer and shear layer flow will be considered, and hence the freestream velocity U_∞ is chosen. The length scale is a relevant length h. Now consider a base state of the system (U_i, P) and a perturbed state of the system $(U_i + u_i', P + p')$, where the primes indicate small perturbations. Both states satisfy the Navier-Stokes equations. If the equations for the base state are subtracted from the equations of the perturbed state, the resulting equations are the nonlinear disturbance equations

$$\frac{\partial u_i}{\partial t} = -U_j \frac{\partial u_i}{\partial x_i} - u_j \frac{\partial U_i}{\partial x_j} - \frac{\partial p}{\partial x_i} + \frac{1}{Re}\nabla^2 u_i - u_j \frac{\partial u_i}{\partial x_j} \tag{2.3}$$

$$\frac{\partial u_i}{\partial x_i} = 0 \tag{2.4}$$

where the primes have been omitted for clarity. The topic of interest is linear stability, and thus equation 2.3 has to be linearized. As mentioned earlier, the added perturbations are small in magnitude. It will be assumed that the product of two small perturbations is significantly small such that the contribution can be neglected.

$$u_i u_j << 1$$

Regarding equation 2.3 this means that the last term on the right hand side is neglected.

Considering the classical canonical base flows (e.g. Couette, Blasius), the base flow $U_i = U(y)\delta_{1i}$ is assumed a parallel flow in the x-direction that is only dependent on the wall-normal position y. Substituting this assumption for U in equation 2.3 the following set of equations is derived:

$$\frac{\partial u}{\partial t} + U\frac{\partial u}{\partial x} + vU' = -\frac{\partial p}{\partial x} + \frac{1}{Re}\nabla^2 u \tag{2.5}$$

$$\frac{\partial v}{\partial t} + U\frac{\partial v}{\partial x} = -\frac{\partial p}{\partial y} + \frac{1}{Re}\nabla^2 v \tag{2.6}$$

$$\frac{\partial w}{\partial t} + U\frac{\partial w}{\partial x} = -\frac{\partial p}{\partial z} + \frac{1}{Re}\nabla^2 w \tag{2.7}$$

where the prime in U' indicates a derivative in y-direction. The continuity equation does not undergo much visual change:

$$\frac{\partial u}{\partial x} + \frac{\partial v}{\partial y} + \frac{\partial w}{\partial z} = 0. \tag{2.8}$$

To be able to solve the perturbation equations in a feasible manner, it is desirable to be able to express this in as little and simple equations as possible. With that goal in mind, the divergence of equations 2.5 through 2.7 is taken, and together with the continuity equation 2.8 an expression for the perturbation pressure is found

$$\nabla^2 p = -2U'\frac{\partial v}{\partial x}. \tag{2.9}$$

Together with equation 2.6, the equation for the perturbation pressure is used to eliminate

p and results in an expression for the normal velocity v

$$\left[\left(\frac{\partial}{\partial t} + U\frac{\partial}{\partial x}\right)\nabla^2 - U''\frac{\partial}{\partial x} - \frac{1}{Re}\nabla^4\right]v = 0 \tag{2.10}$$

with boundary conditions

$$v = v' = 0 \qquad \text{at a solid wall and in the far field} \tag{2.11}$$

and initial condition

$$v(x, y, z, t = 0) = v_0(x, y, z). \tag{2.12}$$

A specific type of disturbance will be considered, namely wavelike disturbances. An ansatz for a wavelike solution can be made in the form

$$v(x, y, z, t) = \tilde{v}(y)e^{i(\alpha x + \beta y - \omega t)}. \tag{2.13}$$

α and β are streamwise and spanwise wavenumbers respectively and ω is the frequency. Substituting this expression 2.13 in equation 2.10 results in an equation for $\tilde{v}$

$$\left[(-i\omega + i\alpha U)(D^2 - k^2) - i\alpha U'' - \frac{1}{Re}(D^2 - k^2)^2\right]\tilde{v} = 0 \tag{2.14}$$

where D^2 is the second derivative in y-direction and

$$k^2 = \alpha^2 + \beta^2 \tag{2.15}$$

The resulting equation 2.14 is called the Orr-Sommerfeld equation (Orr, 1907; Sommerfeld, 1908) and is the basis for temporal and spatial stability analysis.

2.2 Stability analysis

2.2.1 Temporal stability analysis

There are a few different ways to perform stability analysis, based on the method used and specifically in which way a disturbance is introduced. In temporal stability analysis the wavenumbers α and β are considered to be real and the resulting ω will be complex. In spatial stability the frequency ω is considered real and the wavenumbers can now be complex. In Michalke (MICHALKE, 1964) the inviscid problem is studied, which is described by the Rayleigh equation. The Rayleigh equation, rearranged for temporal stability is given by equation 2.16, where $c = \alpha\omega$ is the phase speed, and can be derived from the Orr-Sommerfeld equation by taking the limit for $Re \to \infty$.

$$\left[U\left(\frac{d^2}{dy^2} - \alpha^2\right) - \frac{d^2U}{dy^2}\right]\tilde{v} = c\left(\frac{d^2}{dy^2} - \alpha^2\right)\tilde{v} \tag{2.16}$$

Equation 2.16 is an eigenvalue problem, as is the Orr-Sommerfeld equation in equation 2.14, and can be solved for an array of values for α to find eigenmodes ω, $\beta = 0$. Looking at the ansatz and realizing that ω will be complex valued, i.e. $\omega = \omega_r + i\omega_i$, some conclusions can already be made. If the ansatz is written as in equation 2.18, it can be seen that if $\omega_i > 0$ the eigenmode grows exponentially with time, and thus is unstable. On the other hand, if $\omega_i < 0$ the eigenmode decays exponentially with time and the solution is stable. This problem has an infinite amount of solutions for ω. If a single positive value of ω_i exists, the solution is unstable. In the special case that $\omega_i = 0$ the eigenmode is neutrally stable.

$$v(x, y, z, t) = \tilde{v}(y)e^{i(\alpha x - (\omega_r + i\omega_i)t)} \tag{2.17}$$
$$= \tilde{v}(y)e^{i(\alpha x - \omega_r t)}e^{\omega_i t} \tag{2.18}$$

2.2.2 Spatial stability analysis

For spatial stability analysis a real ω will be assumed, resulting in complex eigenmodes $\alpha = \alpha_r + i\alpha_i$. Decomposing the eigenmodes again the ansatz is now written as in 2.19.

$$v(x, y, z, t) = \tilde{v}(y)e^{i(\alpha_r x - wt)}e^{-\alpha_i x} \tag{2.19}$$

The difference with temporal eigenmodes is the direction of propagation. In time, disturbances can only propagate in positive direction, while in space disturbances can propagate both in positive and negative direction. It is no longer sufficient to look at the value of α_i to draw conclusions of the stability of the system. Now the generalized group velocity v_G needs to be taken into consideration. The generalized group velocity of a certain eigenmode is determined by the response to an impuls on the given system. A positive v_G indicates that this mode contributes to the response of the system downstream of the location of the impulse, or in positive spatial direction. A negative v_G then indicates that the eigenmode contributes to the response of the system upstream of the impulse, or in negative spatial direction. The group velocity is defined in equation 2.20. Eigenmodes with positive group velocities are called α^+ modes. Eigenmodes with negative group velocities are called α^- modes. Stability is determined using both the group velocity and the value of α_i. For α^- modes the same condition holds as for temporal stability, i.e. if $\alpha_i < 0$ the eigenmode grows exponentially in positive spatial direction and if $\alpha_i > 0$ the eigenmode decays exponentially in positive spatial direction. For α^+ modes the exact opposite holds.

$$v_G = \frac{\partial \omega}{\partial \alpha} \tag{2.20}$$

Consider a system governed by the Orr-Sommerfeld equation (2.14) with the hyperbolic tangent profile, equation 2.21, as a base flow.

$$U(y) = \frac{1}{2} + \frac{1}{2} tanh(y) \tag{2.21}$$

Now assuming $\beta = 0$ and rewriting, the Orr-Sommerfeld can be written as a generalised nonlinear eigenvalue problem for α.

$$\left[\frac{-1}{Re}\alpha^4 - iU\alpha^3 + (i\omega + \frac{2}{Re}D^2)\alpha^2 + i(UD^2 - U'')\alpha - i\omega D^2 - \frac{1}{Re}D^4\right]\tilde{v} = 0 \tag{2.22}$$

To solve this nonlinear eigenvalue problem, equation 2.22 will be written as a system of equations, adapted from Cavalieri and Agarwal (CAVALIERI; AGARWAL, 2013).

$$\begin{bmatrix} 0 & I & 0 & 0 \\ 0 & 0 & I & 0 \\ 0 & 0 & 0 & I \\ -F_0 & -F_1 & -F_2 & -F_3 \end{bmatrix} \begin{bmatrix} v \\ \alpha v \\ \alpha^2 v \\ \alpha^3 v \end{bmatrix} = \alpha \begin{bmatrix} I & 0 & 0 & 0 \\ 0 & I & 0 & 0 \\ 0 & 0 & I & 0 \\ 0 & 0 & 0 & F_4 \end{bmatrix} \begin{bmatrix} v \\ \alpha v \\ \alpha^2 v \\ \alpha^3 v \end{bmatrix} \tag{2.23}$$

Where F_i are the coefficients corresponding to α^i. The discrete derivative operator D is discretized using a pseudo-spectral Chebyshev method. The domain is split in $N = 501$ points and is initially defined on the grid $[-1, 1]$, which is stretched with a factor of 20. The domain is stretched to better represent the shear layer behaviour by placing the boundaries far from the high shear region around $y = 0$. The results of the stability analysis can be seen in figures 2.1 and 2.2.

2.3 Comments on the current application

The same code that is used to solve the Orr-Sommerfeld equation in equation 2.23 is used to perform a stability analysis on a base flow obtained in experiments. Where in the previous analysis there was a forcing with temporal frequency ω and the stability was determined in terms of wavenumber α, in the experiment there will also be a spatial forcing, i.e. $\beta \neq 0 \in \mathbb{R}$

For the previous derivation of the Orr-Sommerfeld equation the assumption was made that the base flow is parallel in x-direction and only dependent on the wall-normal position y. In the experiments that have been performed, and will be introduced later, the base

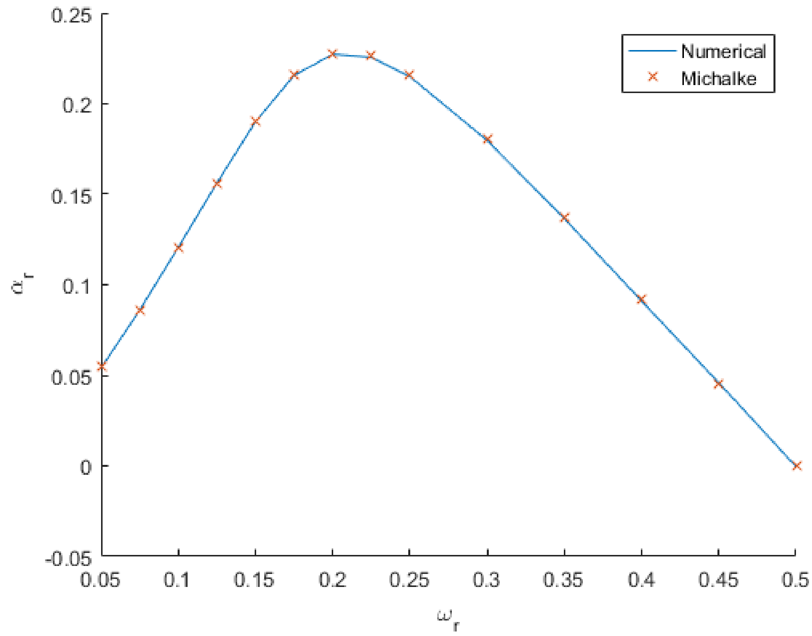

FIGURE 2.1 – Imaginary wavenumber

flow has a spanwise periodic component. That is, the base flow is now expressed as $U_i = U(y,z)\delta_{1i}$. In a similar derivation as before, a set of equations for the 2D base flow is obtained:

$$(-i\omega + i\alpha U)\hat{\nabla}^2\hat{v} + i\alpha U_{zz}\hat{v} + 2i\alpha U_z\hat{v}_z - \alpha U_{yy}\hat{v} \tag{2.24}$$

$$- 2i\alpha U_z\hat{w}_y - 2i\alpha U_{yz}\hat{w} - \frac{1}{Re}\hat{\nabla}^4\hat{v} = 0 \tag{2.25}$$

$$(-i\omega + i\alpha U)\hat{\eta} - U_z\hat{v}_y + U_{zy}\hat{v} + U_y\hat{v}_z + U_{zz}\hat{w} - \frac{1}{Re}\hat{\nabla}^2\hat{\eta} = 0 \tag{2.26}$$

with

$$\hat{\nabla}^2 = \frac{\partial^2}{\partial y^2} + \frac{\partial^2}{\partial z^2} - \alpha^2 \tag{2.27}$$

In the current work the Orr-Sommerfeld equation, in combination with a 1D baseflow will be considered.

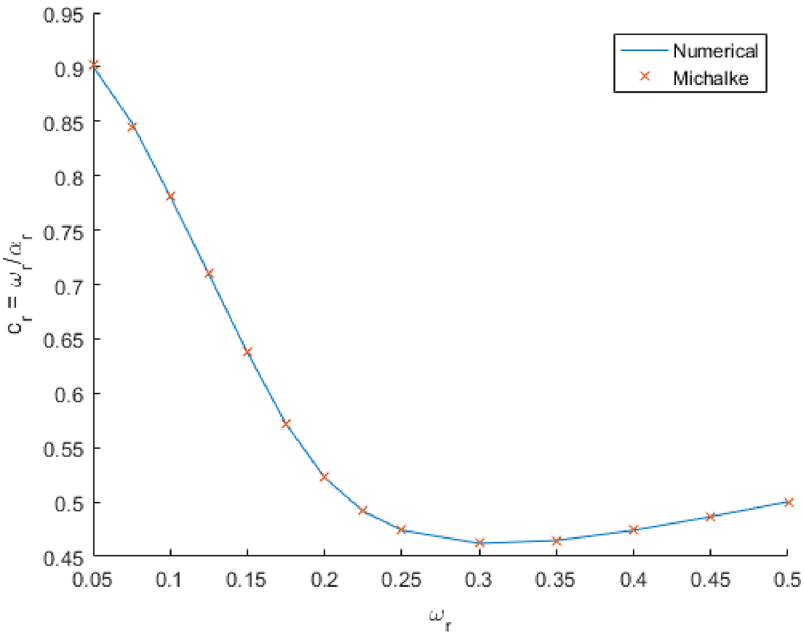

FIGURE 2.2 – Phase velocity

3 Experimental setup

The experiments have been performed in an open circuit wind tunnel at the Prof. Kwei Lien Feng laboratory at ITA. The wind tunnel operates at low speeds ($0 - 33\ m/s$) and with a freestream turbulence level of 0.5%. The test section is similar to the test section used by Ormonde et al (ORMONDE *et al.*, 2018). A sketch of the test section can be seen in figure 3.1. It has a rectangular cross section and has a sudden expansion in the y direction, the classic backwards facing step. A characteristic length scale is defined by the step height h, and a characteristic velocity is given by the freestream velocity U_∞. The expansion ratio of the step is $(H + h)/H = 1.08$ where H is the height of the test section. The span over step height ratio is $e/h = 10.25$, in correspondence with the criterion determined by De Brederode and Bradshaw (BREDERODE; BRADSHAW, 1972) that $e/h > 10$. This criterion ensures a nominally two-dimensional mixing layer by avoiding three-dimensional wall effects at $z = 0$. The test section allows for different splitter plates to be installed. These splitter plates can be designed to serve different purposes and allow for different experiments. Ormonde (ORMONDE *et al.*, 2018) has used a splitter plate with perforations to influence the backflow in the shear layer. In this work a plate with the possibility to place arrays of roughness elements is used. The arrays of circular roughness elements with height k, diameter d and spacing Δz are used as a static flow forcing. The elements can be placed at several streamwise locations upstream from the BFS. A definition of the coordinate system and the roughness elements in an upstream position can be seen in figure 3.2, where the positive x-direction is the streamwise direction, y the wall normal, and z the spanwise coordinate. The total length of the flat plate for boundary layer development is $L = 31.25h$.

3.1 Data acquisition

Data was acquired using hot-wire anemometry. Measurements have been conducted using a single boundary layer hotwire probe, the Dantec 55P05 probe. The wire has a diameter of $5\ \mu m$ and a length of $1.25\ mm$. The viscous length $l^+ = lu_\tau/\nu$, is 63.5. Following (MARUSIC *et al.*, 2010b) a value for the viscous length $l^+ \leq 20$ is sufficient to

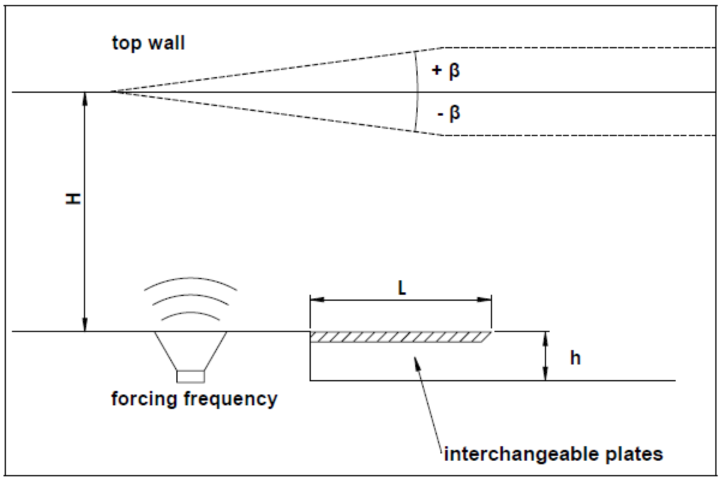

FIGURE 3.1 – Schematic of the test section used, from Ormonde (ORMONDE *et al.*, 2018)

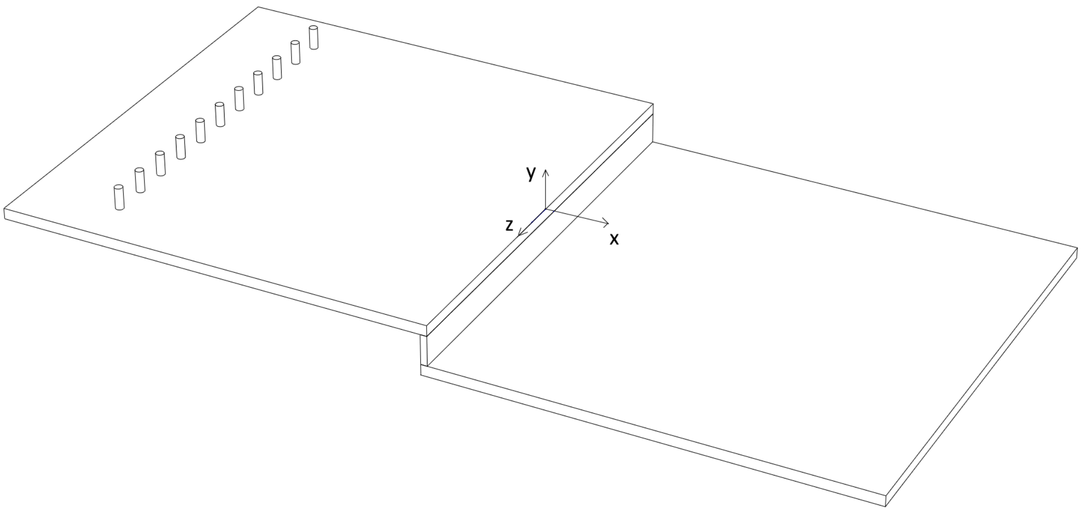

FIGURE 3.2 – Sketch with a definition of the coordinate system and roughness elements

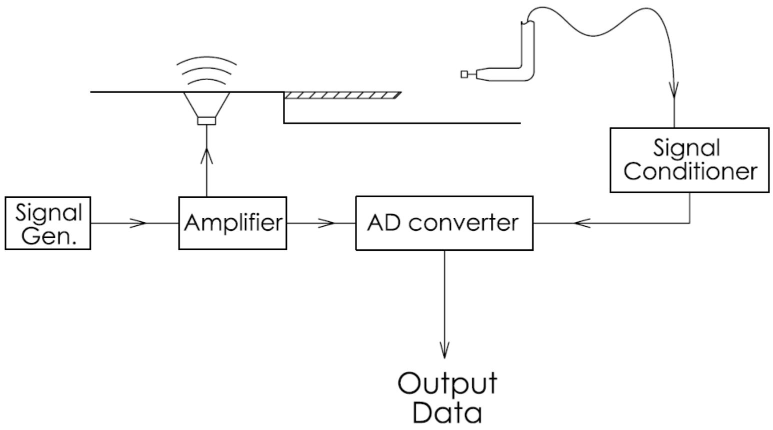

FIGURE 3.3 – Schematic of the data acquisition system, taken from (ORMONDE *et al.*, 2018)

resolve for most of the kinetic energy for wall bounded flows. A higher value will result in measurement errors in the near-wall region. Measurements were done in the x-y plane, at multiple z-locations, at a sample rate of 24 kHz for a duration of 10 s. The signal was conditioned and linearized using DISA 56 series equipment. A low pass frequency filter set at a value of $f_{LP} = 10kHz$ was used to prevent aliasing by frequencies higher than the Nyquist frequency $f_{NY} = \frac{f_{sample}}{2}$. The resulting analog signal is converted to a digital one with a National Instruments NI USB-6009 AD converter. The AD converter has a resolution of 14 bits. A schematic of the setup can be seen in figure 3.3.

3.2 Acoustic forcing

The goal of temporal flow forcing is to excite a Kelvin-Helmholtz mode in the shear layer. The acoustic forcing is applied by using a signal generator. A Edutec model EEL-8003 is used to produce a sine wave. The signal generator is connected to an amplifier. The amplifier, NCA model SA20, sends the amplified signal to a loudspeaker that is connected to the test-section, and to the AD converter. The loudspeaker excites the flow with pressure waves. The hot-wire and forcing signal are recorded simultaneously. This is of importance for the phase-averaging that will be done during the processing.
The previous chapter has introduced the concepts of temporal and spatial stability. The purpose of this acoustic forcing is to impose a single frequency ω_r on the flow which can be tracked, and recognized in the energy spectrum. The analytical tools that have been introduced focus on the 2D flow situation, and so will the forcing. To achieve this, the forcing needs to only excite plane acoustic waves, i.e. other oblique waves are decaying. A condition to ensure only plane propagative waves can be derived using duct acoustics (RIENSTRA; HIRSCHBERG, 2015): $\omega < \pi c_0 / L_{y,z}$, where c_0 is the speed of sound and $L_{y,z}$ is the length in the dimension of its respective subscript. If this condition is satisfied,

all oblique waves will decay in direction of propagation x. The wind tunnel that is used has dimensions $L_y = 0.5m$ and $L_z = 0.41$. This results in a cut-on frequency for oblique waves of $f_{cut-on} = 340Hz$. Only one temporal forcing frequency has been used. The frequency was chosen based on previous research by (**??**), the starting value was $112Hz$ and after finetuning while listening for an acoustic resonance has been set at $110Hz$. The corresponding Strouhal number is $St = \frac{fh}{U_\infty} = 1.3$ The forcing amplitude has been empirically determined, and approved after the forcing frequency was recognized in the energy spectrum of the hot-wire measurements, while the signal arriving from the amplifier still shows little disturbance from the sine function.

3.3 Static forcing

The goal of spatial flow forcing in this experiment is to create the streamwise velocity streaks that have been observed in many previous works, in a structural manner. Roughness elements have been used to force these large scale streamwise structures, as has been done in various earlier work (BAKCHINOV *et al.*, 1995; WHITE, 2002; FRANSSON *et al.*, 2006). Table 3.1 gives an overview of the parameters used in these experiments. White cells indicate values that were not given or could not be derived.

	Bakchinov *et al.*	White *et al.*		Fransson *et al.*	Pujals *et al.*	Ryan *et al.*
$U_\infty(m/s)$	8.2	8	12	7	20	6
$k(mm)$	1.8	0.38	0.38	0.78	12	
$\delta(mm)$	0.72	0.664	0.542	0.29	20	72
k/δ	2.5	0.57	0.70	2.65	0.6	0.13
$d(mm)$	(square) 2	6.35	6.35	2	6	
Re_k	740	45	80	285		
Re_τ						1200
Re_δ				137		28800
Re_L					$1.35 \cdot 10^6$	
$x_k(mm)$	285	225	225	40		
$\Delta z(mm)$	10	12.5	25.0	8	24	
β	0.45	0.24	0.24	0.230		

TABLE 3.1 – Experimental parameters from previous experiments

The roughness elements used in this setup have a cylindrical cross section of diameter d, and a height of k. A total of 11 elements have been used, with equal spacing ΔZ. The elements have been placed at several locations X_0 upstream of the BFS. The specifications of the different configurations of static forcing can be seen in table 3.2. In table 3.3

the parameters that are independent of the configuration can be found. The freestream velocity U_∞, step height h and approach length x_k have been chosen based on previous experiments with the same test section by (ORMONDE *et al.*, 2018). The step height and approach length being determined by the design of the test section. An optimal spatial wavenumber was found by (ANDERSSON *et al.*, 1999) and (LUCHINI, 2000) at $\beta = 0.45$. This optimal disturbance was found for the Blasius profile at high Reynolds numbers. Following this optimal disturbance as basis for determining a spanwise spacing results in a situation where only 3 elements can be placed in the test section. This is similar to what Pujals (PUJALS *et al.*, 2010) encountered. It is thought not wise to follow this assumption because of the influence of the wall effects will be too large. Instead the deciding factor has been a number of elements and in an iterative process the spanwise spacing has been determined using relations and data from (COSSU *et al.*, 2009). From Ormonde (ORMONDE *et al.*, 2018) an estimate for the boundary layer thickness is taken ($\delta = 0.8h$), and the assumption has been made that $\lambda_z/\delta = 1$. In this way a total of eleven roughness elements will be able to fit in the test section. The spanwise spacing has been determined based on the design of the test section. The streamwise spacing was free to determine. In figure 3.4 growth rates and their dependence on the spanwise wavenumber are shown, taken from (**??**). The relation $\delta = 0.223\Delta$ is given, and due to the earlier assumption it holds that $\lambda_z = 0.223\Delta$. Looking at figure 3.4 it can be seen that:

$$\frac{t_{max}U_e}{\Delta} \approx 1 \tag{3.1}$$

and also

$$t_{max}U_e \approx \Delta = \frac{\delta}{0.223} \approx \Delta x \tag{3.2}$$

Now an expression for the streamwise spacing is found. The boundary layer thickness from Ormonde (ORMONDE *et al.*, 2018) together with the expression for the streamwise spacing results in

$$\Delta x = 3.6h. \tag{3.3}$$

Taking this condition as a guidance should ensure that the generated streak is at a maximum at the moment that reaches the BFS. As can be seen in table 3.2 this coincides with configuration *C2*.

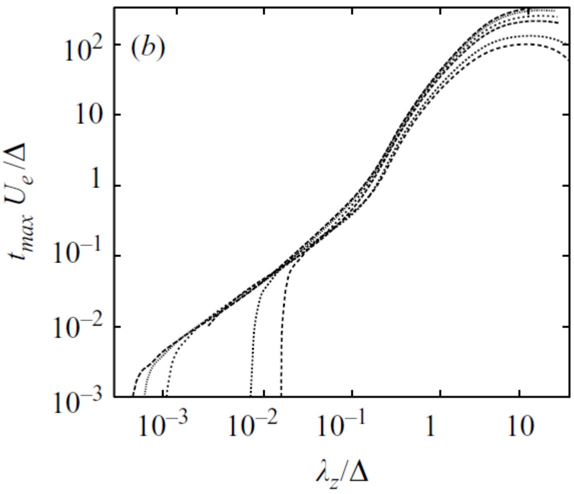

FIGURE 3.4 – (a) Dependence on the spanwise wavenumber $\beta\Delta$ of the maximum growth G_{max} of streamwise uniform ($\alpha = 0$) perturbations for the selected Reynolds numbers Re_{δ_*}. (b) Times t_{max} at which the optimal growths reported in (a) are attained. (COSSU *et al.*, 2009)

ID	X_0	$k(mm)$	k/δ
$C1$	-8	80	2.5
$C2$	-4	80	2.5
$C3$	-1	80	2.5
$C4$	-8	20	0.625
$C6$	-1	20	0.625

TABLE 3.2 – Different pin configurations for static forcing

Re_h	$U_\infty(m/s)$	$h(mm)$	$d(mm)$	x_k	$\Delta z(mm)$	β	n
$5.3 \cdot 10^4$	22.5	40	8	$23.25h$	32	2π	11

TABLE 3.3 – Experimental parameters

3.3.1 Data processing

The recorded hot-wire signal $f(\underline{x}, t)$ is measured in volts. A calibration, using a Betz apparatus and thermometer, is used to convert the signal in volts to meters per second using equation 3.4, where ϕ is an angular coefficient, and c is a linear coefficient.

$$u(\underline{x}, t) = \phi f(\underline{x}, t) + c \tag{3.4}$$

The signal $f(\underline{x}, t)$ is recorded simultaneously with the acoustic forcing signal $g(t)$. Especially for longer time series the generation of a signal may be subject to imperfections, leading to a deviation from a purely sinusoidal wave and frequency drift. To avoid this problem the Hilbert transform may be applied (LUO *et al.*, 2009), which is defined as the convolution of the signal $g(t)$ with the function $1/\pi t$. The Hilbert transform is given in equation 3.5, where **p.v.** is the Cauchy principal value of the improper integral.

$$H(g)(t) = \frac{1}{\pi t} * g(t) = \frac{1}{\pi}\mathbf{p.v.}\int_{-\infty}^{\infty} \frac{g(\tau)}{t-\tau} d\tau \tag{3.5}$$

If the signal $g(t)$ is a sinusoidal or quasi-sinusoidal signal, its Hilbert transform $h(t)$ will be a similar signal, in quadrature with $g(t)$. Another, complex, function can be constructed with as real part the original function $g(t)$ and its complex part the Hilbert transform $h(t)$: $z(t) = g(t) + ih(t)$, and the instantaneous phase of the excitation signal can be extracted. The phase-average $\langle f(\underline{x}, t)\rangle$ of finite signal $f(\underline{x}, t)$ is calculated according to equation 4.15, where $K = t_{record}/\tau$ is the number of cycles present in the acquired signal and $\phi_n = \frac{n2\pi}{N} = \left[\frac{1}{N}2\pi, \frac{2}{N}2\pi, ..., 2\pi\right]$ is the phase, divided into N parts.

$$\langle f(\underline{x}, t)\rangle = \frac{1}{K}\sum_{k=0}^{K}\sum_{n=0}^{N} f(\underline{x}, \phi_n + 2\pi k) \tag{3.6}$$

A Fourier transform is applied to the phase-averaged signal. The Fourier modes are represented by the Fourier coefficients $C_n = A_n + iB_n$ and contain information about the amplitude and phase. C_0 is real valued and is equivalent to the amplitude of the mean, which in this case is zero. The excitation frequency is represented by C_1. This property will be extracted from the phase average to compare with predictions made by linear stability analysis.

4 Results

This chapter will start with general results of the velocity profiles and rms profiles of the total situation. Later the results will be split into two different parts, namely the boundary layer $X < 0$ and the shear layer $X > 0$. The methods used for analysis for the two situations are such different that a separation is needed for clarity.

4.1 Velocity mean and rms overview

Here the main characteristics of the flow before and after encountering the BFS are presented. Results of the velocity profiles will be shown for the baseline case, where there is no forcing in the $z = 0$ plane, and in the $x - y$ planes at $z = 0$ and $z = \Delta z/2$ for the forced situation. The same is true for the rms distributions that will be presented. All measurements have been done for $Re = 5.3 \cdot 10^4$. To avoid cluttering, only figures for situations *'C1'* and *'C4'* will be shown. In figures 4.1 and 4.2 these velocity profiles can be seen. It must be noted that the coordinates at the x-axis only serve as a guidance to show at which location the measurement was taken. The black dashed line corresponds to the centerline, the red crosses correspond to the centerline profile at $z = 0$, and the blue circles correspond to the offcenter plane at $z = \Delta z/2$. In further figures the same markers and colours will be used. Looking at these figures, a couple of pronounced features can be seen. First of all the trivial transition from boundary layer to shear layer from $X = 0$. Another expected feature is the wake region behind the roughness elements. The wake region is defined by a low pressure area directly behind the element, which results in a velocity deficit in the same region. This is only present for in figure 4.1. Comparing the forced profile of *C1* with the baseline profile, the effect of the roughness elements is clearly represented in the lower mean velocity. Comparing the two forced mean profiles, it can be seen that there is a difference around height $Y = 1.5$. This difference is attributed to streaky streamwise behaviour. The streamwise streaky behaviour is more apparent in figure 4.2. The influence of the streaks is seen for all streamwise measurements, both in the boundary layer and 'survive' the BFS and extend well into the shear layer. As mentioned before, the coordinate system has been normalized by the step height. If

$\delta(mm)$	$\delta^*(mm)$	$\theta(mm)$	$H = \frac{\delta^*}{\theta}$	Re_τ	Re_θ
29.96	3.44	2.48	1.38	$1.67 \cdot 10^3$	$3.67 \cdot 10^3$

TABLE 4.1 – Flow properties of the baseline boundary layer prior to detachment $X = -1$

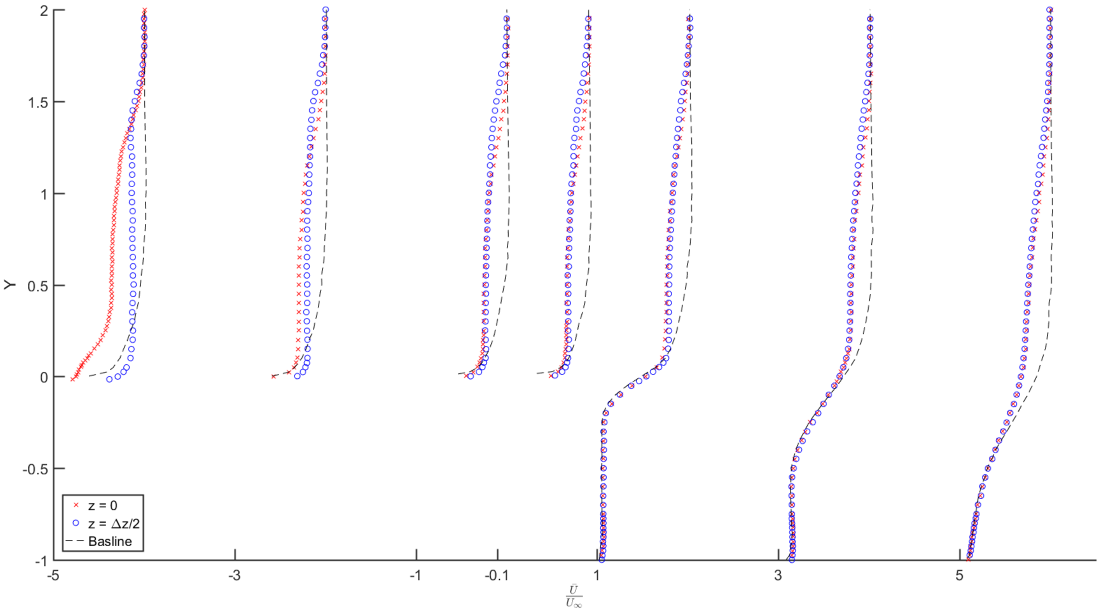

FIGURE 4.1 – Full figure containing streamwise velocity profiles of the baseline (black dashed), centerplane (red crosses) and offcenter plane (blue circles) for configuration *'C1'*

downstream coordinate is expressed in term of boundary layer thickness δ it is seen that the streaks persist up until $\approx 12\delta$ downstream. For roughness elements that are placed inside the boundary layer, the forced effect extends throughout the whole boundary layer in $y-$direction. Table 4.1 shows the properties of the baseline boundary layer prior to detachment at the BFS.

Figures 4.3 and 4.4 show the rms profiles of all streamwise measurement locations. First of all a clear increase in rms value for the region $Y > 0$ can be seen in all profiles. In the shear layer in the region $Y < 0$ an attenuation of the fluctuations is observed, which is more present further downstream, indicating that the streaks could have a stabilizing effect on the shear layer. The rms values for the slow streak decay to freestream values later than the fast streak does. This difference manifests around the upper part of the streak. The same behaviour is observed in figure 4.4. There is slight attenuation of the shear layer fluctuations, and there is a clear region where the rms profiles show different behaviour.

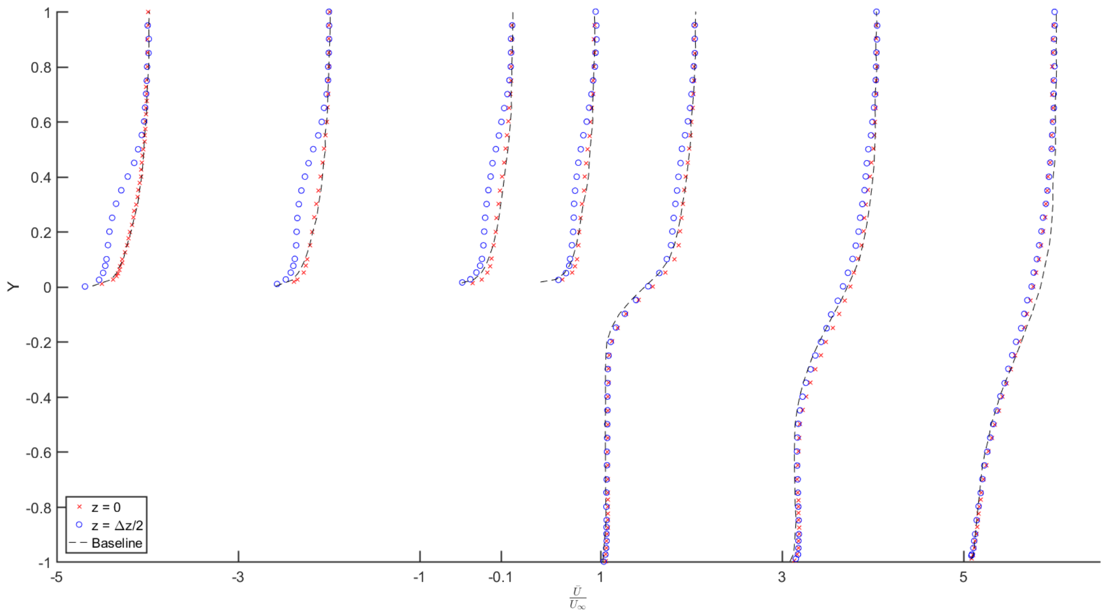

FIGURE 4.2 – Full figure containing streamwise velocity profiles of the baseline (black dashed), centerplane (red crosses) and offcenter plane (blue circles) for configuration *'C4'*

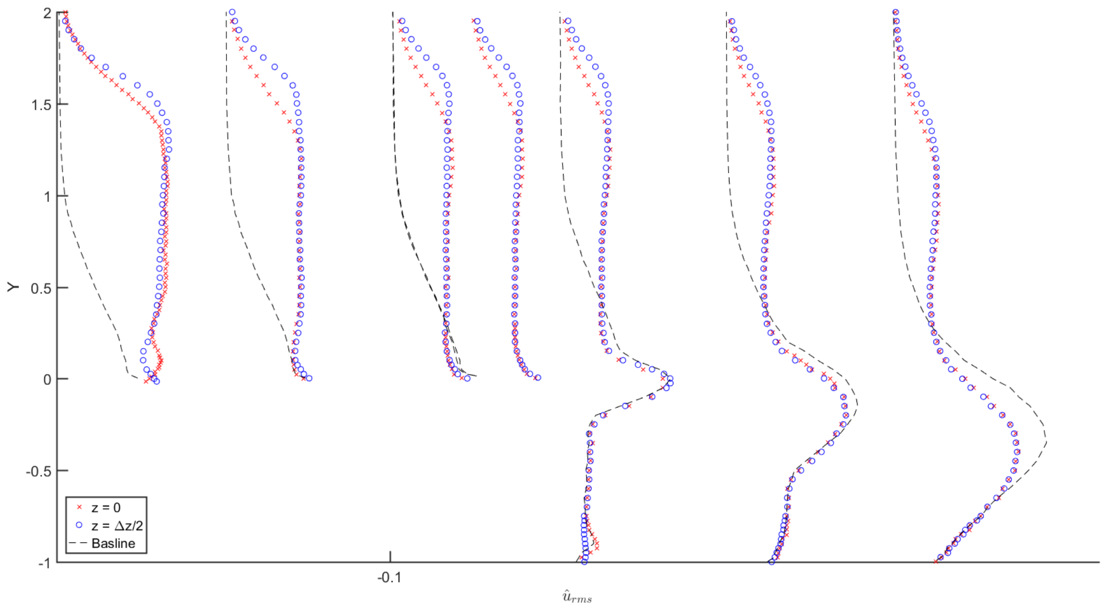

FIGURE 4.3 – Full figure containing streamwise rms distributions of the baseline (black dashed), centerplane (red crosses) and offcenter plane (blue circles) for configuration *'C1'*

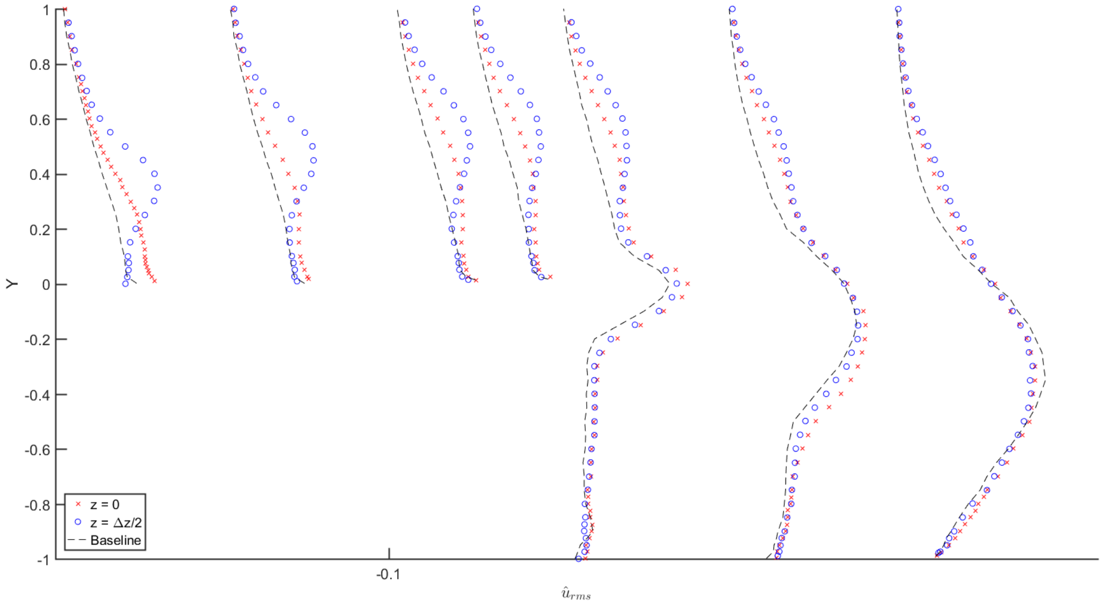

FIGURE 4.4 – Full figure containing streamwise rms distributions of the baseline (black dashed), centerplane (red crosses) and offcenter plane (blue circles) for configuration *'C4'*

4.2 Boundary layer

In this section experimental results of the effect of the forcing on the boundary layer are further studied. Specifically the boundary layer for configuration *C4* at streamwise location $X = -1$ will be considered. Flow properties will be scaled in viscous units. The data acquisition technique that was used, and the experiments that were performed, focused on acquiring velocity data. To determine the friction velocity, oil film interferometry or laser doppler anemometry techniques can be used (JOHANSSON *et al.*, 2005). Due to several limitations, it was not possible to perform these in the current study. To get an approximation of the friction velocity, numerical data for zero pressure gradient turbulent boundary layers from (ÖRLÜ; SCHLATTER, 2013) have been used, together with the relation in equation 4.1 from (OSTERLUND, 2000):

$$c_f = 2\Big[\frac{1}{\kappa}ln(Re_\theta) + C\Big]^{-2} \tag{4.1}$$

where C is a constant and κ is the Von Kármán constant. Data for a zero pressure gradient turbulent boundary layer with a freestream velocity of $U_\infty = 20.0621\ m/s$ and friction velocity of $u_\tau = 0.77614\ m/s$ have been plotted against theoretical values according to Pope (POPE, 2000). The constants of the velocity profile, in inner scaling, for experiments of the baseline case are then empirically determined by looking when the profile has most overlap with the data from (ÖRLÜ; SCHLATTER, 2013). The result for the boundary layer at $X = -3$ can be seen in figure 4.5. These values for the friction velocity are used as constant values for each streamwise position in both the baseline and forced situations. A

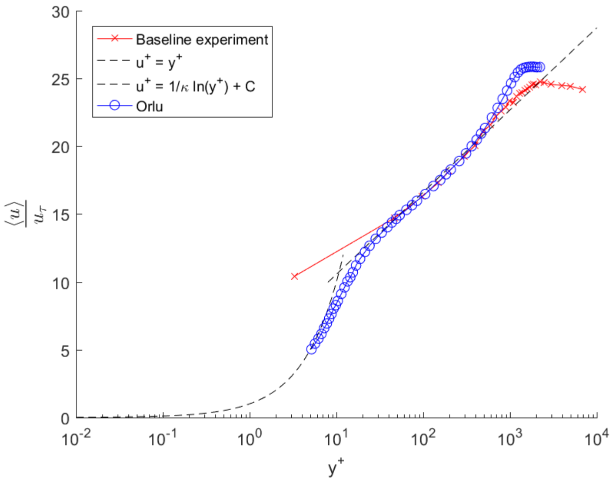

FIGURE 4.5 – Velocity profile for data from (ÖRLÜ; SCHLATTER, 2013), experimental data for a baseline case at $X = -3$, and theoretical values from (POPE, 2000), all in inner scaling

$u_{\tau,Orlu}$	$X = -5$	$X = -3$	$X = -1$	$X = -0.1$
0.77614	0.7614	0.7731	0.7972	0.7966

TABLE 4.2 – Friction velocities empirically determined after matching baseline data with data from Orlu (ÖRLÜ; SCHLATTER, 2013)

friction velocity has been determined for all measurements upstream from the BFS. The friction velocities can be seen in table 4.2. In the previous section the different behaviour of the rms profiles has already been pointed out, and this will be investigated further now. In figure 4.7 The rms profiles at $X = -0.1$ of configuration *C4* are shown. The red crosses show the profile at the centerline, and the blue circles show the profile at the offcenter plane. In outer scaling (in figure 4.4) it was already clear that there is a region where the rms values of the slow streak are higher than those of the fast streak. Inner scaling now shows that the opposite is also happening, but at a position much closer to the wall. This effect has been seen before by Marusic (MARUSIC *et al.*, 2010a) and a schematic representation of this effect can be seen in figure 4.6. The small downward movement that is present in the fast streak convects the present fluctuations toward the wall, creating a region of higher rms near the wall. The opposite is happening for the slow streak. The slow upward movement convects fluctuations away from the wall, creating a region of high rms further away from the wall. It must be noted that the values for very low y^+ have probably been influenced by interaction from the hotwire positioning very close to the wall. The streak amplitude is calculated in the same way as Fransson did (FRANSSON *et al.*, 2004):

$$A_{ST} = \max_{y}[U(y)_{high} - U(y)_{low}]/2 \tag{4.2}$$

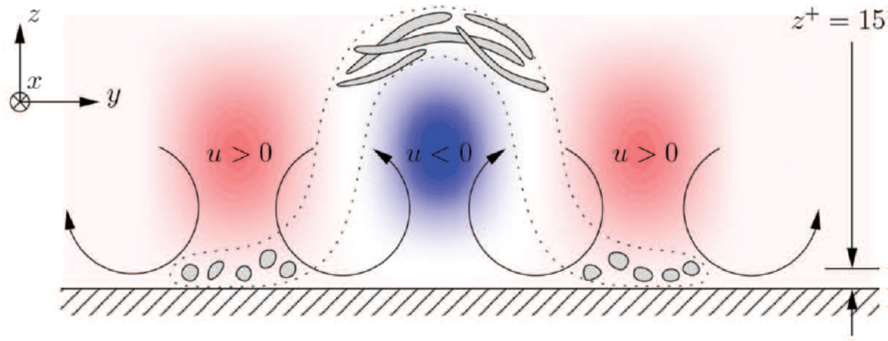

FIGURE 4.6 – Schematic representation of streamwise streaks in spanwise cross-section, from (MARUSIC *et al.*, 2010a)

where $U(y)_{high}$ and $U(y)_{low}$ represent the velocity profiles for the fast and the slow streak respectively. The maximum streak amplitude and its height have been determined for all streamwise positions of the boundary layer. The rms profiles with the location of the maximum streak amplitude can be seen in figures 4.8 through 4.11. The height where the rms profiles cross is approximately the center of the streaks. The streamwise trend is consistent with earlier results, the streaks move away from the wall.

As was mentioned before, the effect of the presence of streaks on the velocity fluctuations has been seen before, and is schematically seen in figure 4.6. However, this has all been seen for turbulent boundary layers where this phenomenon is always present, at a distance very close to the wall ($y^+ \approx 15$). The measurements that are shown in figures 4.7 through 4.11 show the same effect at a much larger distance from the wall, up to $y^+ \approx 2000$. The large scale streaks, also superstructures, are in this way isolated and their properties can be studied. This can provide an easy way to study this phenomenon without the need for a windtunnel like the one used in Marusic (MARUSIC; HUTCHINS, 2008), with an entry length of 27 meters.

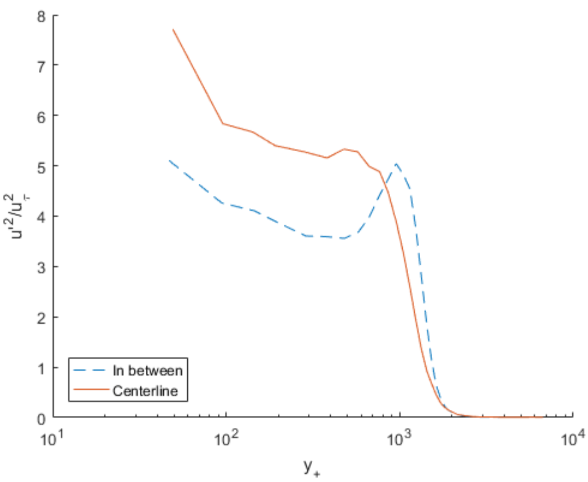

FIGURE 4.7 – Rms profile in viscous units at $X = -0.1$ of configuration *C4*

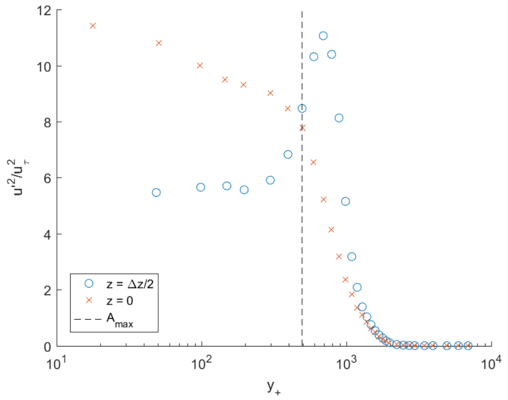

FIGURE 4.8 – Maximum amplitude $X = -5$

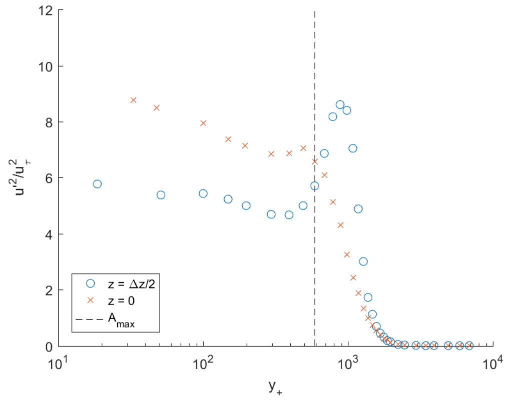

FIGURE 4.9 – Maximum amplitude $X = -3$

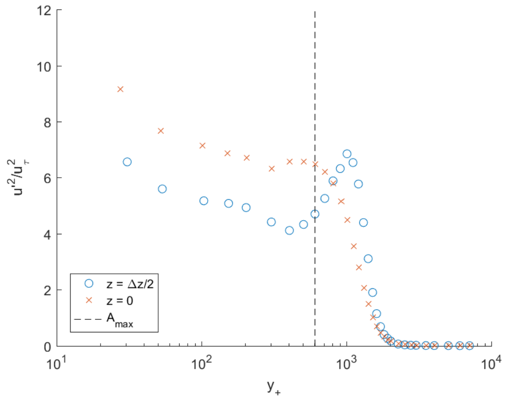

FIGURE 4.10 – Maximum amplitude $X = -1$

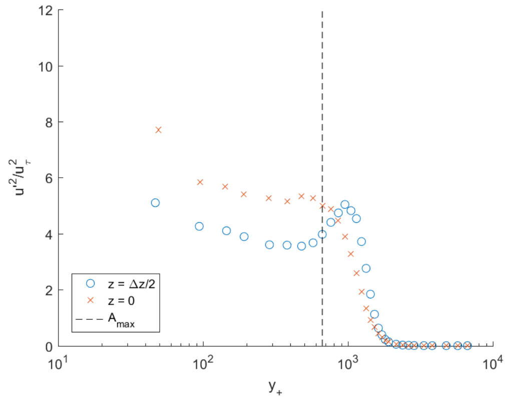

FIGURE 4.11 – Maximum amplitude $X = -0.1$

4.3 Shear layer

In this section the experimental results of the effect of the forcing on the shear layer are further studied. Specifically the shear layer for configuration *C4* at streamwise location $X = 1$ will be considered. The velocity profiles and rms profiles can be seen in figures 4.12 and 4.13. A condition similar to what has been done by Ormonde (ORMONDE *et al.*, 2017) has been applied here as well. The hot-wire measurements cannot measure the direction of the flow, due to the setup, and thus the velocities measured in the region $y < 0$ are measured as positive. No positive velocities are expected below $y = -0.3$, and as such the values of the measured velocities are multiplied with -1, to get an approximation to the backflow. The first thing that is noted is the velocity difference between the centerline profile and the off-center profile, and the baseline. The velocity profiles for the exited flow show a two stage transition in the shear layer. Looking at figure 4.13, the same two stage behaviour can be seen in the rms profiles, in the form of a bump. There is only a slight deviation in the peak value, i.e. higher for the centerline profile, or fast streak, and lower

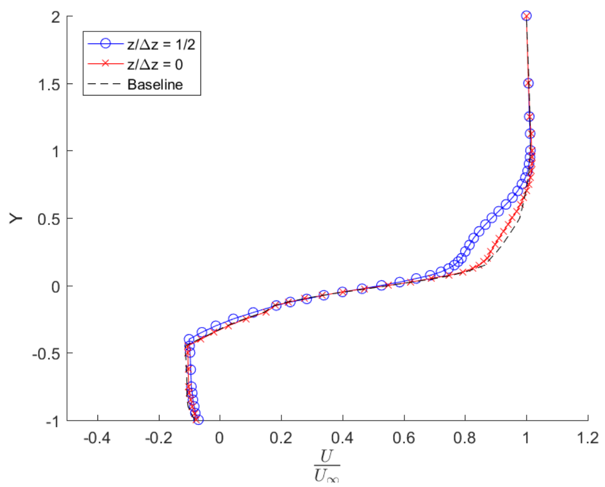

FIGURE 4.12 – Velocity profile for $X = 1$

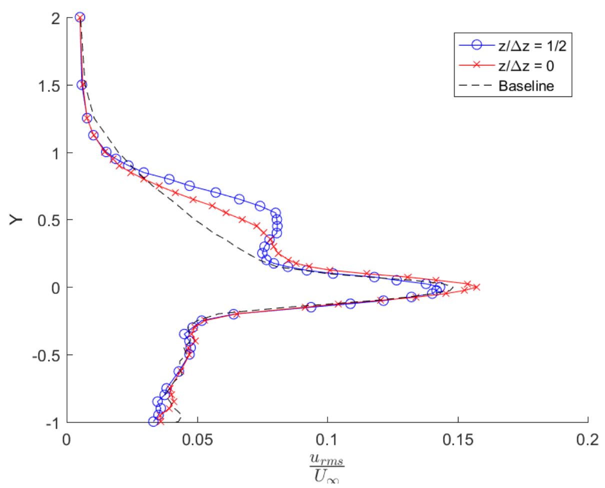

FIGURE 4.13 – Rms profile for $X = 1$

for the off-center profile, or slow streak. The same behaviour as was described by Marusic (MARUSIC *et al.*, 2010a) and observed for the boundary layer can still be observed, the perturbations for the fast streak are more present close to $Y = 0$ and at a certain point of increasing Y there are more perturbations in the slow streak.
Looking at the energy spectrum in figure 4.14 shows that the signal that was forced by the loudspeaker is propagated downstream and recorded by the hotwire.

4.3.1 Linear stability and comparison with forced shear layers

Now that it is confirmed that the disturbance imposed by the loudspeaker propagates to the shear layer, the phase averaging procedure can be applied. The phase averaging is applied as was described earlier in chapter 2, and the first Fourier coefficient can be extracted. The results can be seen in figure 4.15. This result will be compared to the

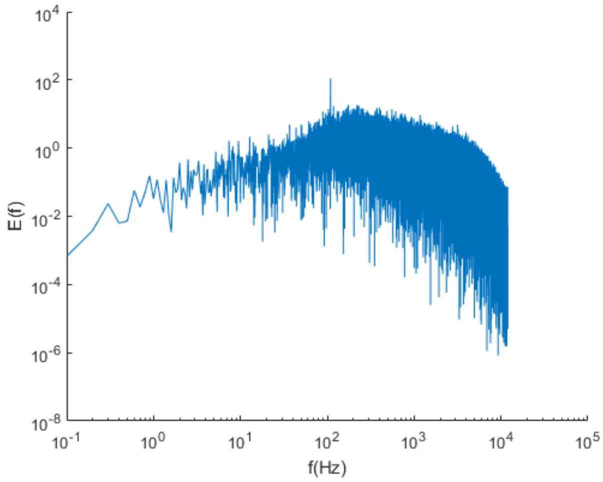

FIGURE 4.14 – Energy spectrum of the recorded signal for $X = 1, \ Y = 0$

eigenfunction of the Kelvin-Helmholtz mode that may be found using the linear stability analysis. The goal is to test if the amplitude of the velocity fluctuations is driven by a linear mechanism.

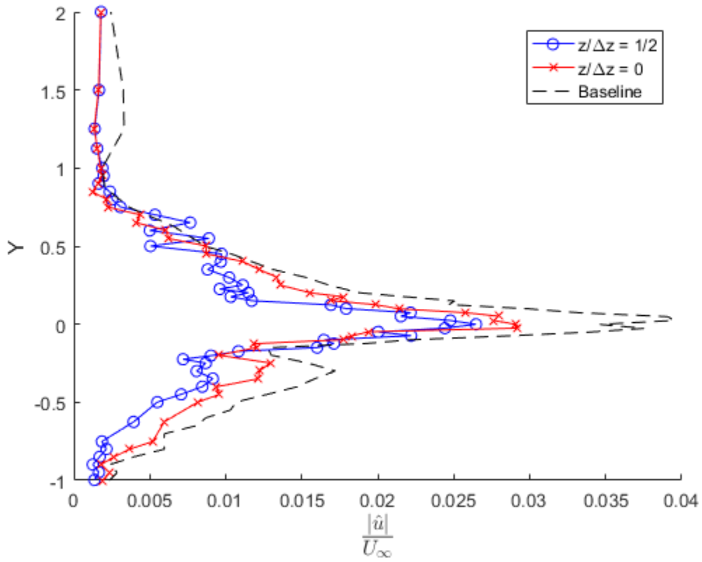

FIGURE 4.15 – Results for the phase averaging procedure for $X = 1$

The result for the spanwise forced shear layer is similar to the baseline, only damped. The peak is in the same location but of lower amplitude, as is the same with the characteristic bump.

Now the mean velocity profile will be used as a base flow for the linear stability analysis. The baseflow is 2D in nature but here the 1D Orr-Sommerfeld from equation 2.22 is be solved. As base flow the average of the two spanwise mean velocity profiles is taken. A continuous approximation of the velocity profile is acquired by using a piecewise cubic hermite interpolating polynomial on the numerical domain, $y \in [-1, 19]$. The interpolated velocity profile can be seen in figure 4.16.

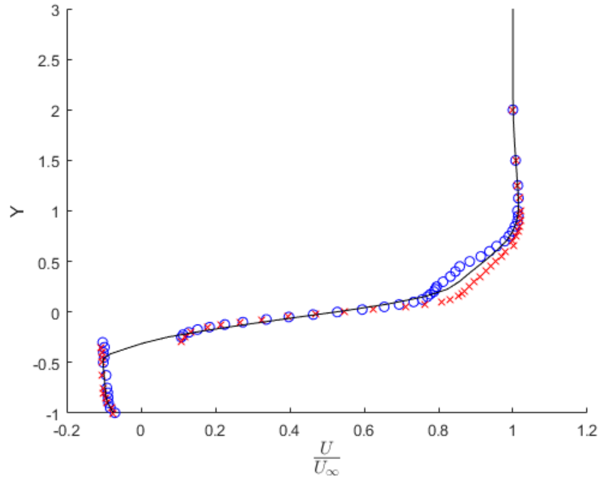

FIGURE 4.16 – Interpolated velocity profile (black solid line), and fast and slow streak velocity profiles (red crosses and blue circles respectively) at $X = 1$

Again the datapoints below $Y = -0.3$ are believed to be negative values due to the present backflow. Like the analysis in chapter two, the system of equations is discretised on a chebyshev grid with $N = 501$ points. After solving the system of equations the resulting eigenspectrum can be found in figure 4.17.

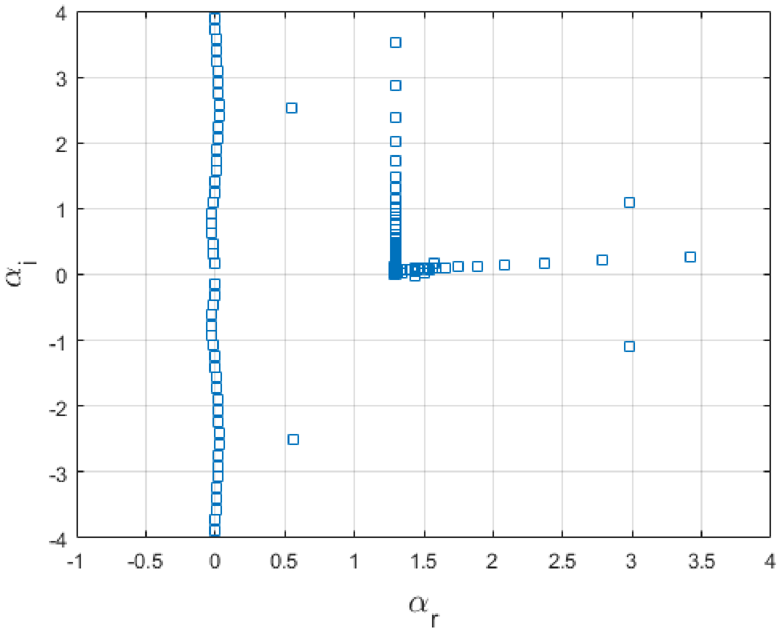

FIGURE 4.17 – Eigenspectrum for the solution of the 1D Orr-Sommerfeld equation

After performing the stability analysis, and checking for the group velocity, there appears one unstable eigenmode, the Kelvin-Helmholtz mode, at $\alpha = 2.98 - 1.089i$. The

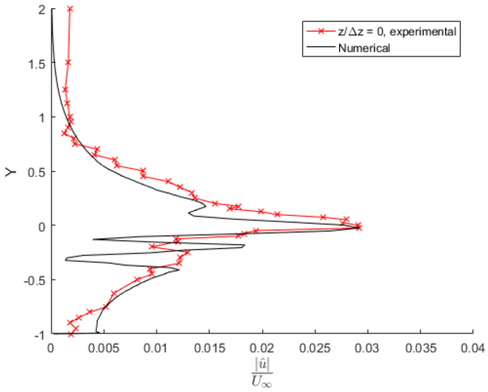

(a) Roughness elements, measurement at $z/\Delta z = 0$

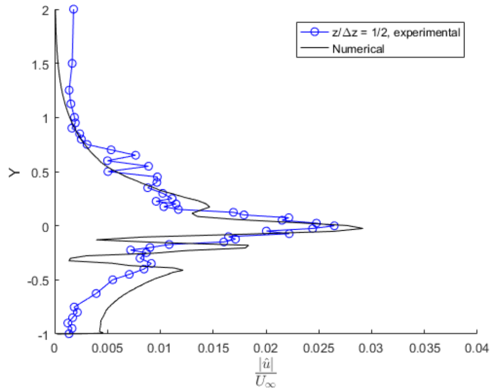

(b) Roughness elements, measurement at $z/\Delta z = 2$

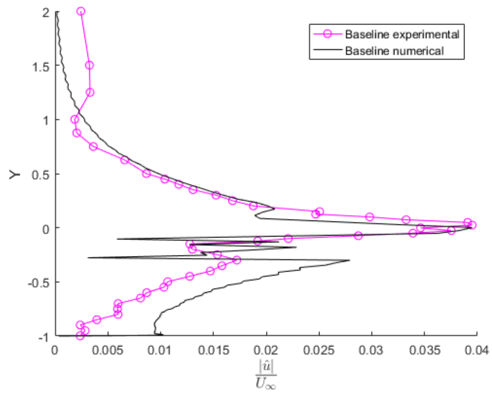

(c) Baseline, measurement at $z/\Delta z = 0$

FIGURE 4.18 – Eigenfunctions from LST and eigenmode responses for the forced (4.18a & 4.18b) and baseline (4.18c) measurements at $X = 1$.

eigenmode $\tilde{v}(y)$ corresponding to this eigenvalue is used to calculated the streamwise disturbances according to the continuity equation, 4.3. The resulting eigenfunction is a solution to the Orr-Sommerfeld equation with arbitrary amplitude and is scaled such that the maximum of $\hat{u}$ is equal to the maximum of u_{KH}, for its relative configuration.

$$\tilde{u} = \frac{i}{\alpha}\frac{d\tilde{v}}{dy} \tag{4.3}$$

In figure 4.18 the results from the LST and the Fourier modes for the base flow from figure 4.16 are shown. A good match is observed. The match for the region $Y > 0$ is very close. The region for negative Y shows discrepancies, which are worst for the baseline case in figure 4.18c. The discrepancies in the region $Y < 0$ may be caused by several effects. The presence of backflow, although an approximation has been made, cannot be captured by a single-wire hotwire probe. Furthermore, the experimental accuracy may contribute to the discrepancy. The interpolated base flow velocity profile in figure 4.16 looks smooth. In the process of solving the Orr-Sommerfeld equation the first and second

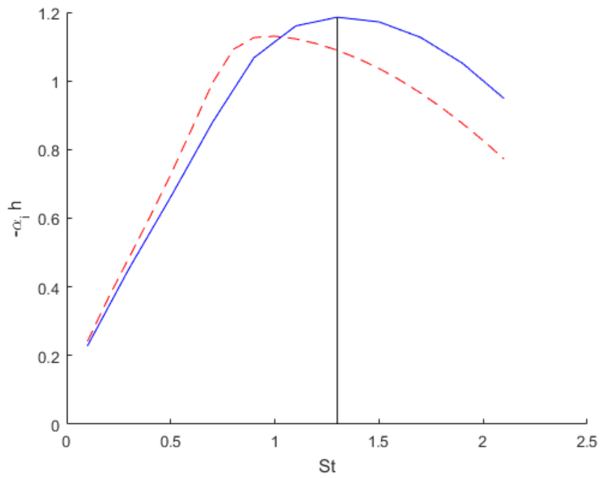

FIGURE 4.19 – Spatial growth rate as a function of Strouhal number, for baseline (blue solid) and forced (red dashed) base flow profile at $X = 1$. Strouhal number for the forcing used in experiments is marked (solid black vertical).

derivatives of the base flow are calculated and in the process of derivation, slight errors are amplified. The exaggerated oscillation around $Y \approx -0.25$ could be due to this effect. Despite the discrepancies, the agreement with the linear stability theory model can provide a theoretical basis for the analysis of the behaviour of coherent structures in these types of flows.

Because it is now known that the linear stability theory can be used to get a decent approximation of the eigenmodes, it can now be extended to calculate the spatial growth rate ($-\alpha_i h$) over a range of Strouhal numbers. These results can be seen in figure 4.19. The flow with the roughness elements shows a slightly larger growth rate for lower frequencies. After Strouhal $St \approx 1.05$ the situation mirrors, and the baseline flow has a larger growth rate for higher Strouhal numbers. This agrees with what was found in the experiments, and was shown in figure 4.15. The linear stability theory is successful in predicting the response of the shear layer to the forcing and the evolution of coherent structures in the shear layer, as the eigenfunctions and the Fourier modes show good agreement.

5 Conclusions and future prospectives

This section serves to summarize the most important results, and draw conclusions. Also prospectives for the future are given, be it possible applications, or directions for future research.

A test section has been designed to force spanwise periodic disturbances on a turbulent boundary layer flow, approaching a backwards facing step configuration. This was both inspired by work on the stabilizing effect of velocity streaks on the transition to turbulence (FRANSSON *et al.*, 2006) and the possibilities provided by the test sections built by and used in (ORMONDE *et al.*, 2018).

The results show that the properties of the boundary layer are changed, i.e. the roughness elements induce spanwise periodic velocity streaks. Once the streaks reach the backwards facing step they remain present. For roughness elements with heights larger than the boundary layer the streaks are induced outside the boundary layer, whereas for roughness elements with heights smaller than the boundary layer thickness the streaks stay inside the boundary layer. After movement downstream of the backward facing step the amplitude of perturbations in the shear layer is lowered with respect to the baseline case, while the thickness of the shear layer increases.

The phase averaging analysis shows a decrease in presence of Kelvin-Helmholtz mode in the shear layer. The Kelvin-Helmholtz mode being the most unstable mode in a flow, this result indicates a stabilizing effect of streaks on the shear layer. This result has been achieved while using suboptimal disturbances. Optimal disturbances may prove to have a bigger effect on the damping of Kelvin-Helmholtz modes.

The stability analysis was successful in predicting the behaviour of the dominant mode in the shear layer. There are still discrepancies between the LST result and the dominant mode, which is attributed to the uncertainty in the region $Y < 0$ because of the inability to measure backflow with the current setup. Another contributing factor to discrepancies may be the fact that here the base flow was approximated as one dimensional in nature, i.e. steady in both x- and z-directions, and the Orr-Sommerfeld equation for a one dimensional base flow was solved.

As mentioned in the previous chapter, the overall amplitude of the rms in the shear layer is reduced when streamwise streaks are introduced to the shear layer. In this work the focus has been on dynamical flow properties, but an acoustic investigation may yield new insights on reducing turbulent noise in shear layers. The reduced velocity perturbations may hint at a reduced amplitude of noise. The increased shear layer thickness can provide the possibility for larger wavelength disturbances to be present in the shear layer, resulting in a general lower frequency noise. It is suggested to design an experimental setup using the parameters of this work, for a jet, where acoustic measurements are possible. If the prediction of lower frequency noise is confirmed this may ultimately provide a useful insight for the design of jet engines and their produced jet noise.

Bibliography

ADAMS, E. W.; JOHNSTON, J. P. Effects of the separating shear layer on the reattachment flow structure Part 1: Pressure and turbulence quantities. **Experiments in Fluids**, v. 408, p. 400–408, 1988.

ADAMS, E. W.; JOHNSTON, J. P. Effects ofseparatingshearlaer onthe reattachment flow structure Part 2: Reattachment lenght and wall shaer stress. **Experiments in Fluids**, v. 6, p. 493–499, 1988. ISSN 0723-4864.

ANDERSSON, P.; BERGGREN, M.; HENNINGSON, D. S. Optimal disturbances and bypass transition in boundary layers. **Physics of Fluids**, v. 11, n. 1, p. 134–150, 1999. ISSN 10706631.

BAKCHINOV, A. A.; GREK, G. R.; KLINGMANN, B. G.; KOZLOV, V. V. Transition experiments in a boundary layer with embedded streamwise vortices. **Physics of Fluids**, v. 7, n. 4, p. 820–832, 1995. ISSN 10706631.

BARENBLATT, G. I. Scaling laws for fully developed turbulent shear flows Part 1 Basic hypotheses and analysis. **Journal of Fluid Mechanics**, Cambridge University Press, v. 248, p. 513–520, 1993. ISSN 1469-7645.

BARENBLATT, G. I.; CHORIN, A. J.; HALD, O. H.; PROSTOKISHIN, V. M. Structure of the zero pressure gradient turbulent boundary layer. **Proceedings of the National Academy of Sciences**, National Acad Sciences, v. 94, n. 15, p. 7817–7819, 1997. ISSN 0027-8424.

BREDERODE, V. de; BRADSHAW, P. Three dimensional flow in normally two dimensional separation bubbles. **Imperial College, Aeronautical Report**, Imperial College of Science and Technology, p. 72–19, 1972.

CANTWELL, B. J. Organized Motion in Turbulent Flow. **Annual Review of Fluid Mechanics**, v. 13, n. 1, p. 457–515, 1981. ISSN 0066-4189. Disponível em: <http://www.annualreviews.org/doi/10.1146/annurev.fl.13.010181.002325>.

CAVALIERI, A.; AGARWAL, A. The effect of base-flow changes in Kelvin-Helmholtz instability. **19th AIAA/CEAS Aeroacoustics Conference**, n. May, p. 27–29, 2013. Disponível em: <http://arc.aiaa.org/doi/abs/10.2514/6.2013-2088>.

COSSU, C.; BRANDT, L. Stabilization of Tollmien-Schlichting waves by finite amplitude optimal streaks in the Blasius boundary layer. **Physics of Fluids**, v. 14, n. 8, 2002. ISSN 10706631.

COSSU, C.; PUJALS, G.; DEPARDON, S. Optimal transient growth and very large-scale structures in turbulent boundary layers. **Journal of Fluid Mechanics**, v. 619, p. 79–94, 2009. ISSN 00221120.

CROW, S. C.; CHAMPAGNE, F. H. Orderly structure in jet turbulence. **Journal of Fluid Mechanics**, v. 48, n. 3, p. 547–591, 1971. ISSN 14697645.

EATON, J. K.; JOHNSTON, J. P. A Review of Research on Subsonic Turbulent Flow Reattachment. **AIAA Journal**, v. 19, n. 9, p. 1093–1100, 1981. ISSN 0001-1452. Disponível em: <http://arc.aiaa.org/doi/10.2514/3.60048>.

FRANSSON, J. H.; BRANDT, L.; TALAMELLI, A.; COSSU, C. Experimental and theoretical investigation of the nonmodal growth of steady streaks in a flat plate boundary layer. **Physics of Fluids**, v. 16, n. 10, p. 3627–3638, 2004. ISSN 10706631.

FRANSSON, J. H.; TALAMELLI, A.; BRANDT, L.; COSSU, C. Delaying transition to turbulence by a passive mechanism. **Physical Review Letters**, v. 96, n. 6, p. 1–4, 2006. ISSN 10797114.

FRANSSON, J. H. M.; BRANDT, L.; TALAMELLI, A.; COSSU, C. Experimental study of the stabilization of Tollmien-Schlichting waves by finite amplitude streaks. **Physics of Fluids**, v. 17, n. 5, p. 1–15, 2005. ISSN 10706631.

FREYMUTH, P. On transition in a separated laminar boundary layer. **Journal of Fluid Mechanics**, v. 25, n. 4, p. 683–704, 1966. ISSN 14697645.

HUSSAIN, A. K. M. F.; REYNOLDS, W. C.; REYNOLDS, C. The mechanics of an organized wave in turbulent shear flow. **Journal of Fluid Mechanics**, v. 41, p. 241–258, 1970. ISSN 0022-1120.

JOHANSSON, T.; MEHDI, F.; SHIRI, F.; NAUGHTON, J. W. Skin Friction Measurements using Oil Film Interferometry and Laser Doppler Anemometry. **AIAA Paper**, p. 1–15, 2005. Disponível em: <http://arc.aiaa.org/doi/pdf/10.2514/6.2005-4673>.

KENDALL, J. Experimental study of disturbances produced in a pre-transitional laminar boundary layer by weak freestream turbulence. In: **18th Fluid Dynamics and Plasmadynamics and Lasers Conference**. [S.l.: s.n.], 1985. p. 1695.

KENDALL, J. M. The effect of small-scale roughness on the mean flow profile of a laminar boundary layer. In: **Instability and transition**. [S.l.]: Springer, 1990. p. 296–302.

KLEBANOFF, P. S. Effect of free-stream turbulence on a laminar boundary layer. In: **Bulletin of the American Physical Society**. [S.l.: s.n.], 1971. v. 16, n. 11, p. 1323—-+.

LUCHINI, P. Reynolds-numbers-independent instability of the boundary layer over a flat surface : optimal perturbantions. **J. Fluid Mech.**, v. 404, p. 289–309, 2000.

LUO, H.; FANG, X.; ERTAS, B. Hilbert Transform and Its Engineering Applications. **AIAA Journal**, v. 47, n. 4, p. 923–932, 2009. ISSN 0001-1452. Disponível em: <http://arc.aiaa.org/doi/10.2514/1.37649>.

MARUSIC, I.; HUTCHINS, N. Study of the log layer structure in wall turbulence over a very large range of reynolds number. **Flow, Turbulence and Combustion**, v. 81, n. 1-2, p. 115–130, 2008. ISSN 13866184.

MARUSIC, I.; MATHIS, R.; HUTCHINS, N. Predictive model for wall-bounded turbulent flow. **Science**, v. 329, n. 5988, p. 193–196, 2010. ISSN 00368075.

MARUSIC, I.; MCKEON, B. J.; MONKEWITZ, P. A.; NAGIB, H. M.; SMITS, A. J.; SREENIVASAN, K. R. Wall bounded turbulent flows at high Reynolds numbers Recent advances and key issues. **Physics of Fluids**, v. 22, n. 6, p. 1–24, 2010. ISSN 10706631.

MICHALKE, A. On the inviscid instability of the hyperbolictangent velocity profile. **Journal of Fluid Mechanics**, v. 19, n. 4, p. 543–556, 1964. ISSN 14697645.

MICHALKE, A. On spatially growing disturbances in an inviscid shear layer. **Journal of Fluid Mechanics**, v. 23, n. 3, p. 521–544, 1965. ISSN 14697645.

NICKELS, T. B.; MARUSIC, I.; HAFEZ, S.; HUTCHINS, N.; CHONG, M. S. Some predictions of the attached eddy model for a high Reynolds number boundary layer. **Philosophical Transactions of the Royal Society of London A: Mathematical, Physical and Engineering Sciences**, The Royal Society, v. 365, n. 1852, p. 807–822, 2007. ISSN 1364-503X.

ÖRLÜ, R.; SCHLATTER, P. Comparison of experiments and simulations for zero pressure gradient turbulent boundary layers at moderate Reynolds numbers. **Experiments in Fluids**, v. 54, n. 6, 2013. ISSN 07234864.

ORMONDE, P. C.; CAVALIERI, A. V. G.; ROBERTO, G. A.; ANA, S. Passive control of coherent structures in a modified backwards facing step flow. **Experiments in Fluids**, Springer Berlin Heidelberg, v. 0, n. 0, p. 0, 2018. ISSN 1432-1114. Disponível em: <http://dx.doi.org/10.1007/s00348-018-2543-y>.

ORMONDE, P. C.; CAVALIERI, V. G.; SILVA, R. G. A.; AVELAR, A. C. Stabilizing effects of a perforated splitter plate on a backwards-facing step. **AIAA Journal**, p. 1–15, 2017.

OSTERLUND, J. M. **Experimental studies of zero pressure gradient turbulent boundary layer flow**. [S.l.]: Mekanik, 1999.

OSTERLUND, J. O. PhysFluids A note on the overlap region in turbulent boundary layers.pdf. v. 12, n. 1, p. 1–4, 2000.

POPE, S. B. Turbulent Flows. **Journal of Turbulence**, v. 1, p. 771, 2000. ISSN 1468-5248.

PUJALS, G.; DEPARDON, S.; COSSU, C. Drag reduction of a 3D bluff body using coherent streamwise streaks. **Experiments in Fluids**, v. 49, n. 5, p. 1085–1094, 2010. ISSN 07234864.

RIENSTRA, S. E. U. o. T.; HIRSCHBERG, A. E. U. o. T. An Introduction to Acoustics. **Book**, v. 0, n. 0, p. 296, 2015. ISSN 00029505.

RYAN, M. D.; ORTIZ-DUENAS, C.; LONGMIRE, E. K. Effects of Simple Wall Mounted Cylinder Arrangements on a Turbulent Boundary Layer. **AIAA Journal**, v. 49, n. 10, p. 2210–2220, 2011. ISSN 0001-1452. Disponível em: <http://arc.aiaa.org/doi/abs/10.2514/1.J051012>.

SCHMID, P. J.; HENNINGSON, D. S. **Stability and Transition in Shear Flows**. [s.n.], 2001. ISSN 0040-1706. ISBN 978-1-4612-6564-1. Disponível em: <http://link.springer.com/10.1007/978-1-4613-0185-1>.

SINHA, S. N.; GUPTA, a. K.; OBERAI, M. Laminar separating flow over backsteps and cavities. I - Backsteps. **AIAA Journal**, v. 20, n. 3, p. 370–375, 1982. ISSN 0001-1452.

SMITS, A. J.; MCKEON, B. J.; MARUSIC, I. High Reynolds Number Wall Turbulence. **Annual Review of Fluid Mechanics**, v. 43, n. 1, p. 353–375, 2011. ISSN 0066-4189. Disponível em: <http://www.annualreviews.org/doi/10.1146/annurev-fluid-122109-160753>.

WHITE, E. B. Transient growth of stationary disturbances in a flat plate boundary layer. **Physics of Fluids**, v. 14, n. 12, p. 4429–4439, 2002. ISSN 10706631.

ZAGAROLA, M. V.; SMITS, A. J. Mean flow scaling of turbulent pipe flow. **Journal of Fluid Mechanics**, Cambridge University Press, v. 373, p. 33–79, 1998. ISSN 1469-7645.

Appendix A - Other experimental configurations

In this appendix results for the other experimental configurations will be discussed. The experiments have been conducted with the same experimental parameters, except for the element height k and upstream position of the elements, as described in table 3.2. These results have not been analyzed in the same quantitative manner as has been described in the main text. This is because the preliminary results show largely similar behaviour. Although figures for configurations *C1* and *C4* have been shown, they are repeated here.

A.1 Velocity and rms profiles

Figures A.1 through A.5 show the velocity profiles for different streamwise locations for the different experimental configurations. Figures A.6 through A.10 show the rms profiles. It must be noted that the coordinates at the x-axis only serve as a guidance to show at which location the measurement was taken. As was discussed in the main text, the roughness elements create streamwise velocity streaks. For configurations *C1*, *C2* and *C3*, the streaks are created at a height somewhat below the tip of the roughness element at $Y = 2$. In figures A.2 and A.3 the wake behind the roughness elements can still be seen. This is one of the reasons these configurations were not the best suitable options for thorough analysis. It must be noted that after some development length the wake decays and streaks remain. Similar effect as have been described are expected to be present. For configuration *C6* the same thing is true. A wake is present, which decays after some development length, after which streaks remain. The attenuation of the velocity profile for the shear layer in configuration *C6* is bigger than for configuration *C4*. However for both configurations with the roughness elements located at $X = -0.1$, the amplitude of the velocity fluctuations is not attenuated. This can be because the undeveloped streaks and wake are directly introduced to the shear layer. The velocity fluctuations for the intermediate configuration *C2* are of lower magnitude than for fully developed streaks.

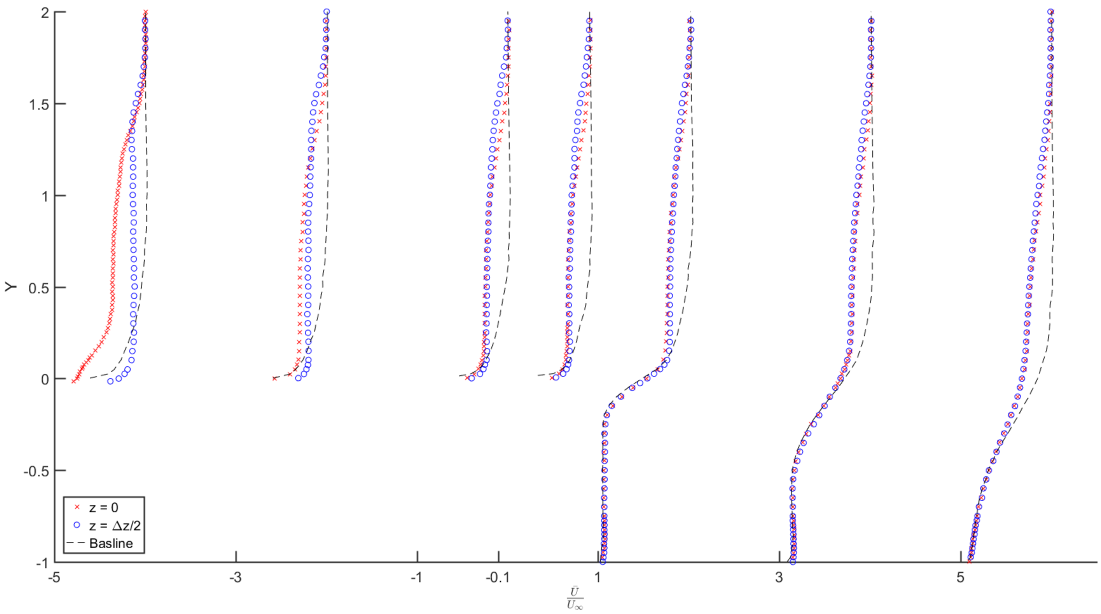

FIGURE A.1 – Velocity profiles at different streamwise locations for configuration *C1*

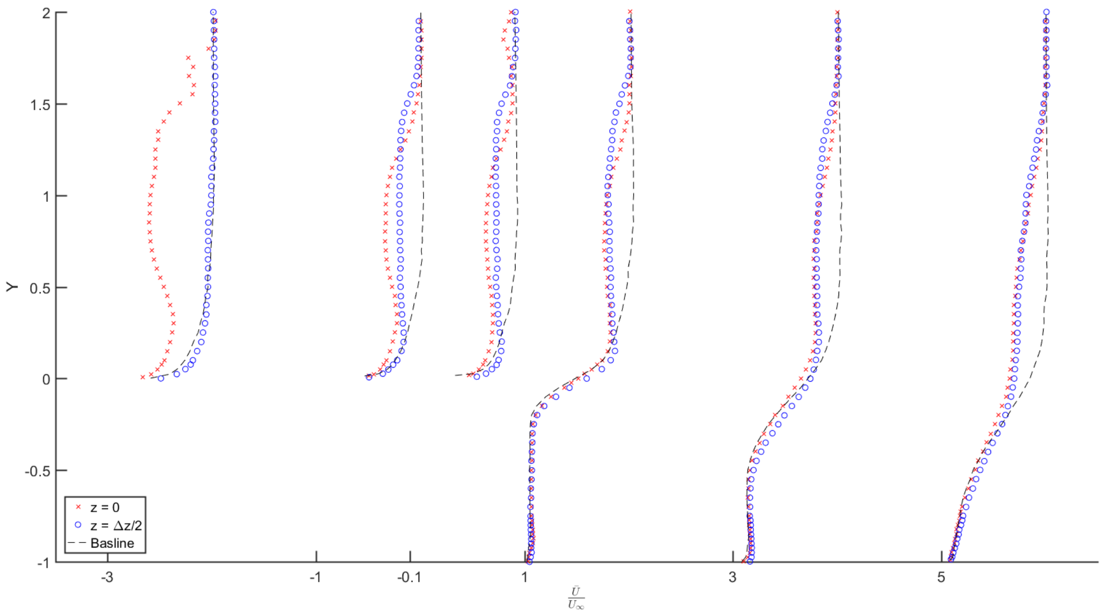

FIGURE A.2 – Velocity profiles at different streamwise locations for configuration *C2*

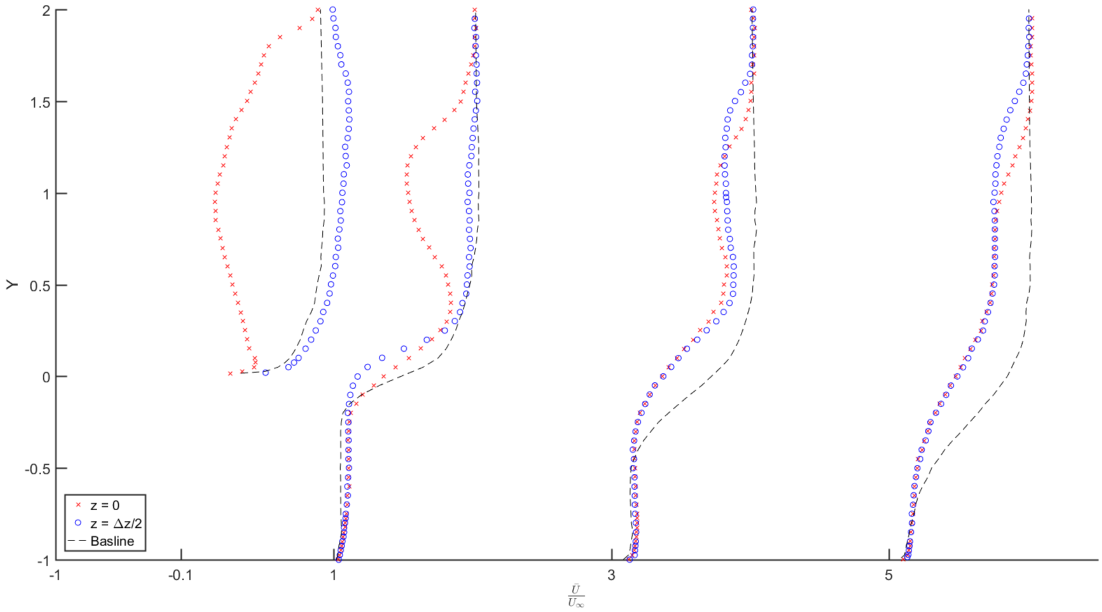

FIGURE A.3 – Velocity profiles at different streamwise locations for configuration *C3*

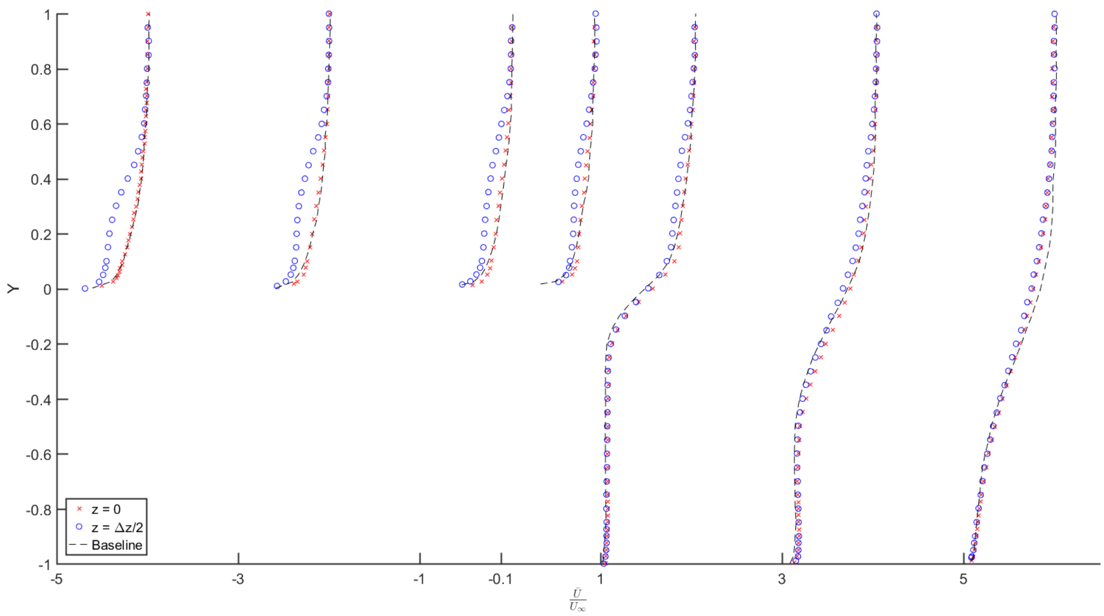

FIGURE A.4 – Velocity profiles at different streamwise locations for configuration *C4*

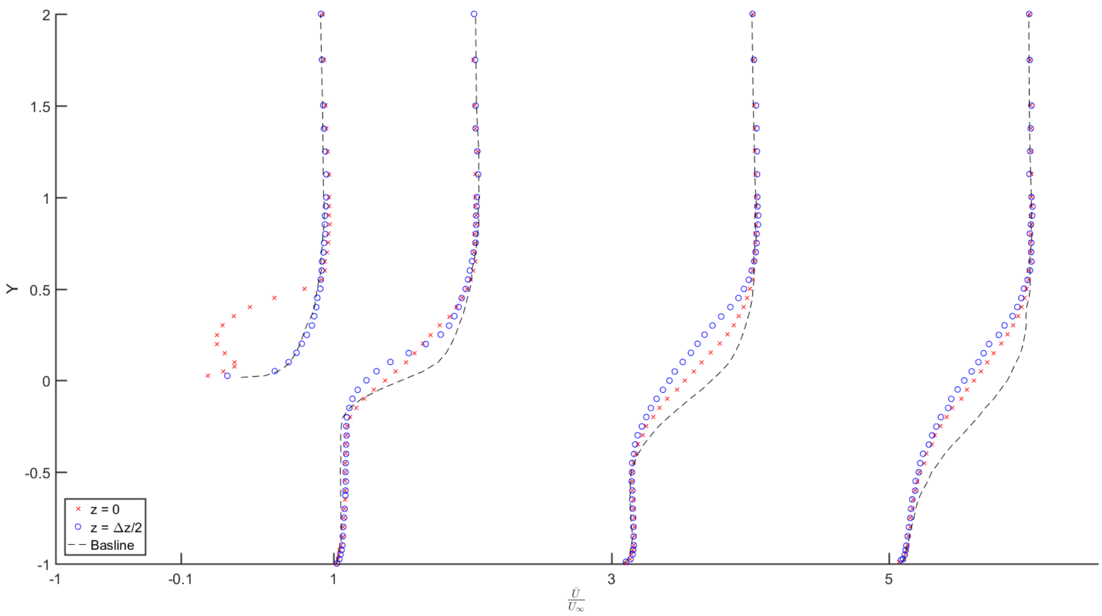

FIGURE A.5 – Velocity profiles at different streamwise locations for configuration *C6*

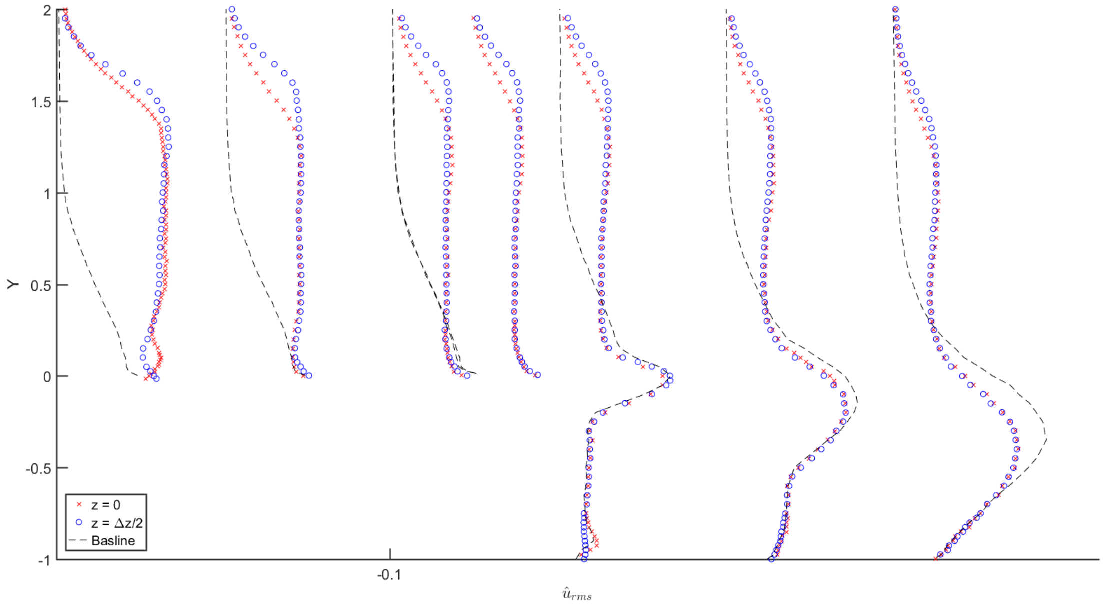

FIGURE A.6 – Rms profiles at different streamwise locations for configuration *C1*

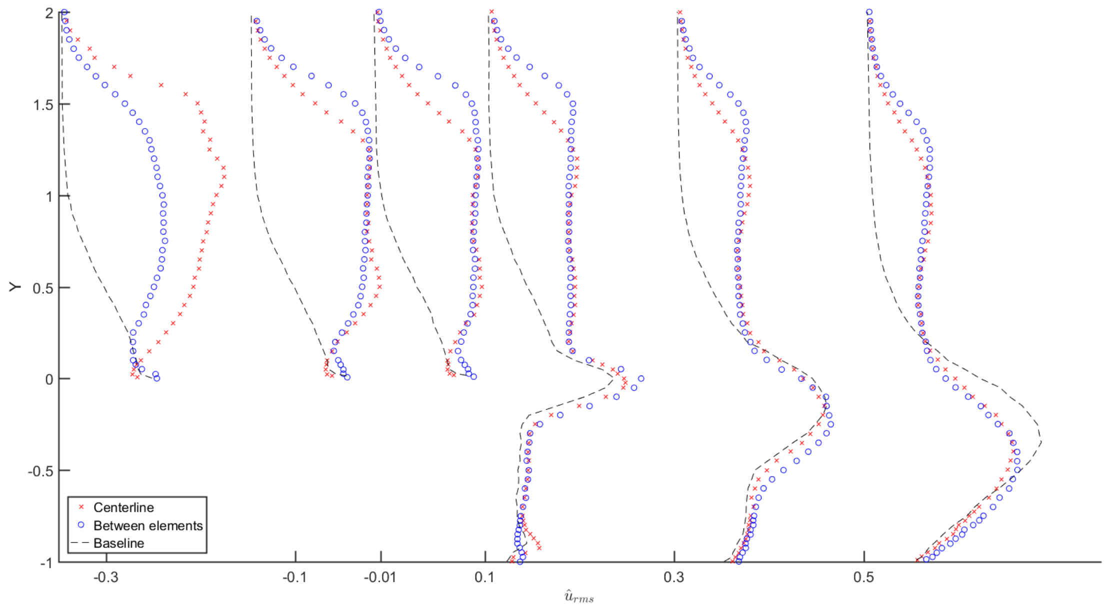

FIGURE A.7 – Rms profiles at different streamwise locations for configuration *C2*

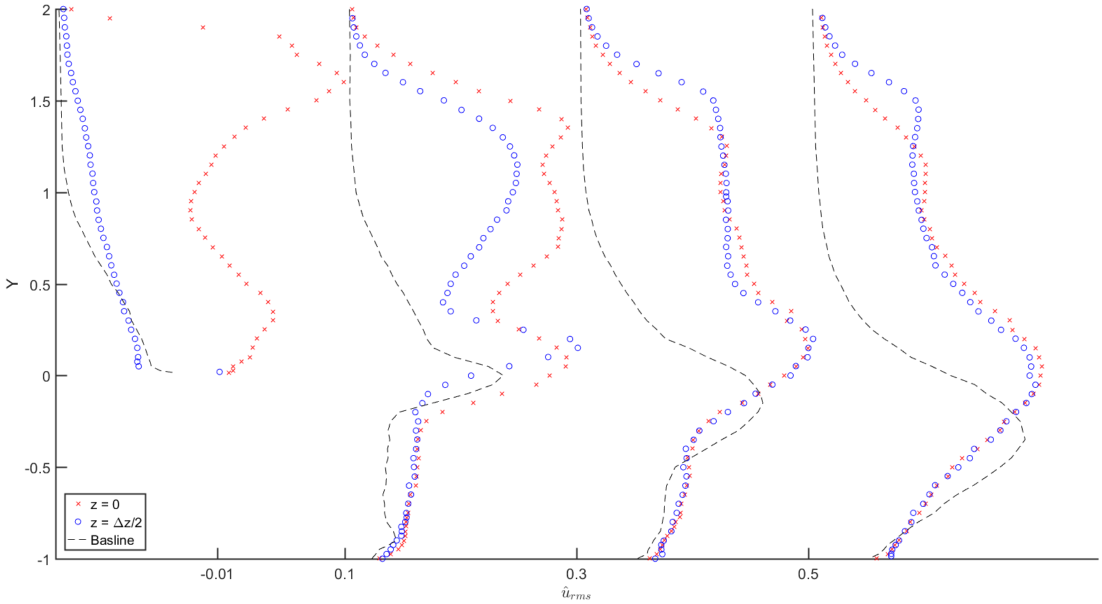

FIGURE A.8 – Rms profiles at different streamwise locations for configuration *C3*

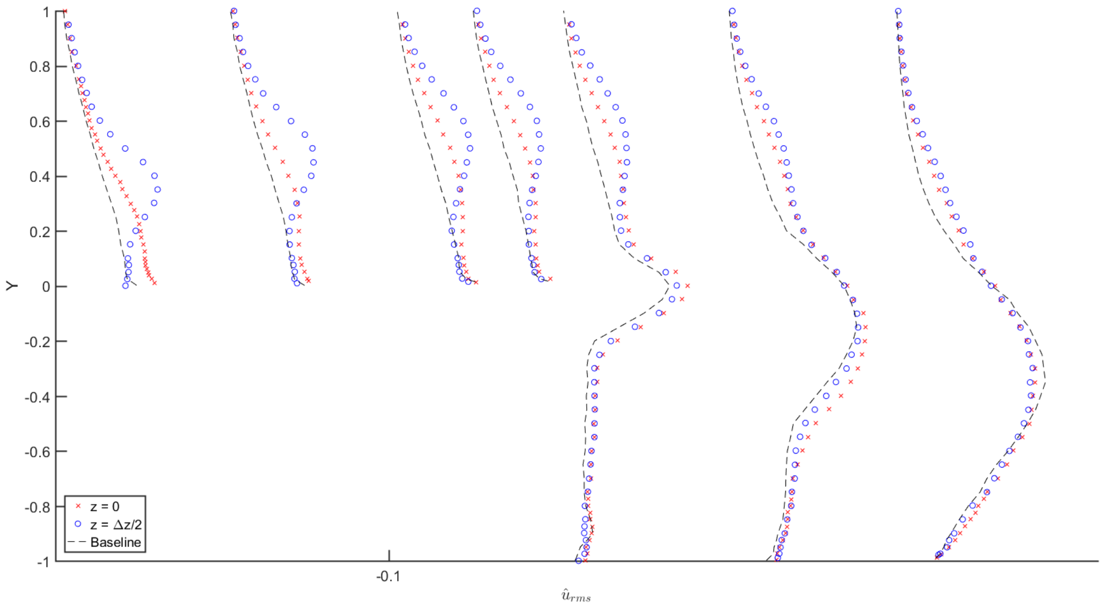

FIGURE A.9 – Rms profiles at different streamwise locations for configuration *C4*

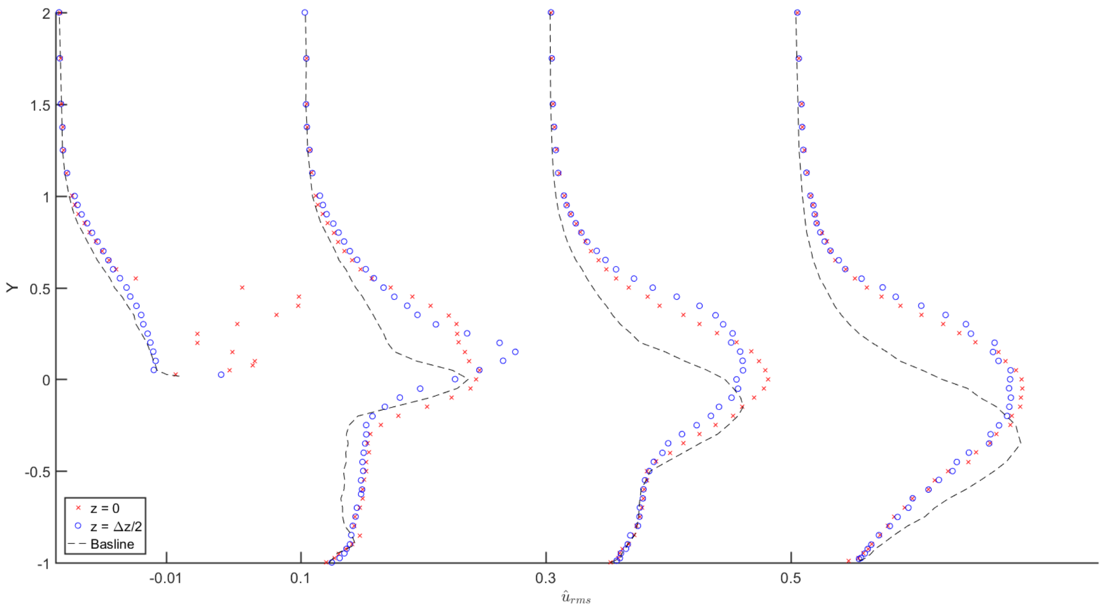

FIGURE A.10 – Rms profiles at different streamwise locations for configuration *C6*

FOLHA DE REGISTRO DO DOCUMENTO

1. CLASSIFICAï¿½ï¿½O/TIPO	2. DATA	3. DOCUMENTO Nï¿½	4. Nï¿½ DE Pï¿½GINAS
DM	8 de Agosto de 2018	DCTA/ITA/DM-018/2015	55

5. Tï¿½TULO E SUBTï¿½TULO:

Influence of suboptimally forced streamwise streaks on the turbulent boundary layer and shear layer

6. AUTOR(ES):

Willem Pieter Waasdorp

7. INSTITUIï¿½ï¿½O(ï¿½ES)/ï¿½RGï¿½O(S) INTERNO(S)/DIVISï¿½O(ï¿½ES):

Instituto Tecnológico de Aeronáutica – ITA

8. PALAVRAS-CHAVE SUGERIDAS PELO AUTOR:

Cupim; Cimento; Estruturas

9. PALAVRAS-CHAVE RESULTANTES DE INDEXAï¿½ï¿½O:

Cupim; Dilema; Construção

10. APRESENTAï¿½ï¿½O: **(X) Nacional** **( ) Internacional**

ITA, São José dos Campos. Curso de Mestrado. Programa de Pós-Graduação em Engenharia Aeronáutica e Mecânica. Área de Sistemas Aeroespaciais e Mecatrônica. Orientador: Prof. Dr. Adalberto Santos Dupont. Coorientadora: Prof^{a}. Dr^{a}. Doralice Serra. Defesa em 05/03/2015. Publicada em 25/03/2015.

11. RESUMO:

Lorem ipsum dolor sit amet, consectetur adipiscing elit. Vestibulum tempus elit nunc, in scelerisque ex scelerisque mattis. Mauris auctor dui id ultrices efficitur. Praesent varius ligula et bibendum accumsan. Praesent malesuada pretium dui, quis ultrices dolor eleifend fermentum. Donec sit amet dictum nunc. Mauris lobortis semper eleifend. Praesent fringilla viverra dolor fermentum auctor. Nulla porta tristique aliquam. Suspendisse convallis felis non odio varius, nec sollicitudin libero porta. Morbi consectetur dapibus sem at gravida. Nunc dictum pharetra cursus. Proin cursus, nunc nec luctus auctor, lorem quam vestibulum ipsum, sit amet vehicula nisl purus eu est. Ut suscipit rhoncus sem, nec egestas dolor sodales sed. Sed convallis blandit lorem et tempus. Nullam imperdiet velit nulla, ut tincidunt arcu vestibulum mattis.

Nunc sit amet porttitor justo, ut placerat dolor. Vestibulum pellentesque cursus posuere. In mollis lectus sit amet lacus semper aliquet. Morbi blandit ornare ante et consequat. Sed vitae metus neque. Mauris elementum viverra turpis non gravida. Orci varius natoque penatibus et magnis dis parturient montes, nascetur ridiculus mus. Quisque sit amet quam viverra, tincidunt ipsum auctor, iaculis quam. Nam consequat tellus at lorem pulvinar, at fermentum lectus viverra. In sed orci a nulla posuere tincidunt. Aliquam ac odio nec lacus tincidunt semper ultricies at diam. Donec tempor nisl nulla, tristique fringilla mi bibendum fermentum. Praesent pharetra, tellus a malesuada viverra, nisl lectus commodo mi, non efficitur justo nisi nec sem.

12. GRAU DE SIGILO:

(X) OSTENSIVO **( ) RESERVADO** **( ) SECRETO**